Phase Error Analysis of Arrayed Waveguide Gratings using Gaussian Beam Approximation of Guided Mode Profiles

A THESIS

submitted by

SIDHARTH RAVEENDRAN

for the award of the degree

of

MASTER OF SCIENCE

(by Research)

DEPARTMENT OF ELECTRICAL ENGINEERING.
INDIAN INSTITUTE OF TECHNOLOGY MADRAS.

August 2015

THESIS CERTIFICATE

This is to certify that the thesis titled **Phase Error Analysis of Arrayed Waveguide Gratings using Gaussian Beam Approximation of Guided Mode Profiles**, submitted by **Sidharth Raveendran**, to the Indian Institute of Technology, Madras, for the award of the degree of **Master of Science**, is a bonafide record of the research work done by him under my supervision. The contents of this thesis, in full or in parts, have not been submitted to any other Institute or University for the award of any degree or diploma.

Dr. Bijoy Krishna Das
Research Guide
Associate Professor
Dept. of Electrical Engineering
IIT-Madras, 600 036

Place: Chennai, India

Date: Mon 11th Apr, 2016

Dedicated to my parents

ACKNOWLEDGEMENTS

I would like to thank my research adviser Dr. Bijoy Krishna Das for the guidance during my work. His guidance has been helping me to develop technical and professional skills and to stay motivated always. I wish to thank my General Test Committee Prof. Harishankar Ramachandran and Prof. Prem B. Bisht for their valuable advice and suggestions.

The Integrated Optoelectronics group at IIT Madras was always supportive and the positive feedback from them always helped me. I specially thank Sujith for his help in various stages of my research and helping me with my fabrication. I thank all my colleagues Sakthivel, Shantanu, Harish, Gaurang, Narendran, Solomon, Sundar, Saket, Sumi, Riddhi, Vivek, Ramesh, Parimal, Mandar, Deepak, Rashmi, Seetha, Sireesha, Srivatsa, Chaitanya, Karthik, Dadavali, Cebin and Jaseem for their moral support and help during various stages of my research. I would also like to wish very best for their future endeavors. I also thank Akhil, Anvar, Praveen Paul, George, Anoop, Sanak, Sreejith, Nikhil and Sarath for making my stay at IIT Madras a pleasant one.

Last but not the least I would like to thank my parents for their unconditional love and support.

ABSTRACT

KEYWORDS: Arrayed Waveguide Gratings, Dense Wavelength Division Multiplexing, Silicon On Insulator, Optical Interconnects, Phase Error

Arrayed Waveguide Gratings (AWGs) are useful as MUX/DEMUX for fiber optic Dense Wavelength Division Multiplexing (DWDM) applications and can also be used in Silicon On Insulator (SOI) based optical interconnect technologies. The high index contrast of SOI waveguides allow us to make very compact structure, but found to be highly sensitive to fabrication related imperfections. Uniformity in arrayed waveguide dimensions and/or effective indices are key factors for the realization of SOI based AWG structures.

In this work, we designed a nearly polarization independent AWG in SOI with 2-μm device layer thickness and a compact AWG in SOI with 220-nm device layer thickness. The devices can (de-)multiplex 8 channels with 100 GHz spacing and has a free spectral range of 800 GHz - uniform over a wide range of wavelength encompassing C+L bands. AWG on 2-μm-SOI (220-nm-SOI) consists of an array of 40 (28) waveguides with a differential length of $\triangle L$ = 109 (85.09) μm. Phase error due to width variations in the arrayed waveguides is a huge problem for AWGs especially in high index contrast platforms like SOI. Hence, study on phase error analysis of AWG is very essential to study the fabrication tolerance of the device. However, the most popular commercial FDTD design tools demand huge computational budget for simulating an AWG. Therefore, a rugged design tool is necessary to analyze the effect of imperfection in the waveguide geometry on the spectral characteristics of AWG . A semi-analytical method using Gaussian beam approximation of guided mode profile has been developed to analyze the spectrum of arrayed waveguide gratings on different platforms. This method has been validated using RSoft BeamPROP and published experimental results. The method is found to be accurate and faster compared to the commercial numerical methods. The phase error analysis of the designed AWGs has been carried out using this

method. It has been found that for AWG fabricated on 2-μm-SOI (220-nm-SOI), the tolerable width variation is $\pm$ 13 nm ($\pm$ 2 nm) to have a crosstalk less than -10 dB. The proposed AWG on 2-μm-SOI has been fabricated using i-line lithography (365 nm), followed by reactive ion etching (SF_6 : Ar :: 20 sccm : 20 sccm, Pressure : 200 mTorr, RF Power : 150 W). The width variation introduced by the fabrication in the arrayed waveguides were more than 100 nm which was above the tolerable limit to get a satisfactory performance. Improved fabrication techniques like e-beam lithography and deep UV lithography (193 nm) can be used to get a better structural uniformity compared to i-line lithography technique. Post fabrication trimming using UV rays can also be used to reduce the non-uniformity in arrayed waveguides.

TABLE OF CONTENTS

ACKNOWLEDGEMENTS **ii**

ABSTRACT **iii**

LIST OF TABLES **vii**

LIST OF FIGURES **x**

ABBREVIATIONS **xi**

NOTATION **xiii**

1 Introduction **1**

1.1 Motivation 1

1.2 Research Objective 3

1.3 Thesis Organization 3

2 Theory and Design **5**

2.1 Working principle 5

2.2 Design Parameters 6

2.3 Design with 2-μm-SOI 10

2.3.1 Single Mode Waveguide 11

2.3.2 Input FPR 12

2.3.3 Output FPR 15

2.3.4 Arrayed waveguides 16

2.3.5 Optimized design parameters 18

2.4 Design with 220-nm-SOI 20

2.4.1 Single Mode waveguide 21

2.4.2 Input FPR 21

2.4.3 Output FPR 23
2.4.4 Arrayed waveguides 23
2.4.5 Optimized design parameters 24
2.5 Summary 24

3 Modeling and Phase Error Analysis 26
3.1 Modeling 26
3.1.1 Gaussian beam approximation at input FPR 32
3.1.2 Gaussian beam superposition at output FPR 35
3.2 Phase Error Analysis 36
3.3 Summary 40

4 Fabrication with i-line Contact Lithography 41
4.1 Photomask Design and Fabrication 41
4.2 Photolithography and Process Optimization 44
4.3 Summary 52

5 Conclusions 53
5.1 Summary 53
5.2 Future Scope of work 54

LIST OF TABLES

2.1 Optimized design parameters of AWG on 2-μm-SOI. 19

2.2 Optimized design parameters of AWG on 220-nmSOI. 25

4.1 Specifications of the mask plate 43

4.2 Spin coating parameters of S1813 G2 44

4.3 Optimized etching recipe 45

4.4 Optimized descum recipe 48

LIST OF FIGURES

2.1 Scheme of conventional AWG. The device consists of Rowland circle geometry. The input/output waveguides are placed on the circumference of a circle (Rowland circle) which has a radius half of that of the circle (Grating circle) where the arrayed waveguides are placed. . . 5

2.2 Input/output FPR model. f is the focal length of FPR, D_i is the separation between arrayed waveguides, D_o is the separation between output waveguides, i is the number of arrayed waveguide, V and W are the focusing points at the output focal plane and O is the reference point at which x = 0. It is assumed that the light from different arrayed waveguides are accumulated at a distance x from the reference point O. . . 7

2.3 Schematic cross-section view of SOI rib waveguide, W is the rib height, H is the rib height and h is the slab height. W, H and h can be carefully chosen to ensure single mode guiding. 11

2.4 Waveguide dispersion relation for extracting waveguide parameters for single mode operation of 2-μm-SOI. For W > 1.6 μm the effective index of first order modes are greater than the slab modes and hence the waveguide will be multimoded. 12

2.5 Simulated mode profiles of the rib waveguide fo H = 2 μm, h = 1 μm (a) W = 1 μm (b) W = 1.5 μm. 13

2.6 Theoretical junction loss at input FPR - arrayed waveguide junction as a function of separation between arrayed waveguides (D_i). 13

2.7 Light collection efficiency of the arrayed waveguides at the inpt FPR - arrayed waveguide junction as a function of number of arrayed waveguides (N). 14

2.8 list entry 16

2.9 Schematic representation of losses in a 90^0 bend. 17

2.10 Calculated mode profiles of a straight and a 90^0 bend waveguide (radius 100 μm) on 2-μm-SOI using Lumerical mode solver. 17

2.11 list entry 18

2.12 3D simulation result of the designed AWG for the parameters shown in Table 2.1 using Rsoft-BeamPROP. 20

2.13 Waveguide dispersion relation for extracting waveguide parameters for single mode operation of 220-nm-SOI. 21

2.14 Theoretical junction loss at input FPR - arrayed waveguide junction as a function of separation between arrayed waveguides (D_i). 22

2.15 Light collection efficiency of the arrayed waveguides at the inpt FPR - arrayed waveguide junction as a function of number of arrayed waveguides (N). 22

2.16 Crosstalk and Rowland circle radius as a function of output waveguide separation (D_o) for AWG fabricated on 220-nm-SOI. A separation value of 300 nm gives a crosstalk $\sim$ -28 dB. 23

2.17 Bend loss of a 90^0 bend for different bend radii for waveguides on 220-nm-SOI. For a particular bend radius, loss for TE polarization is less compared to TM polarization. 24

3.1 Scheme of the AWG used for modeling: three different colours are used for representing the phase-fronts of three channels $\lambda_1, \lambda_c, \lambda_N$; FPR - free propagation region. 27

3.2 (a) Mode profile of a rib waveguide (TE polarization) with W = 1.6 μm, H = 2 μm, h = 1 μm; (b) Mode profile of a photonic wire waveguide (TE polarization) with W = 0.5 μm, H = 0.22 μm; (c) Comparison of 1D mode profiles of rib waveguide (TE polarization) obtained using full vectorial mode solver and Gaussian fit for W = 1.6 μm, H = 2 μm, h = 1 μm; (d) Comparison of 1D mode profiles of photonic wire waveguide (TE polarization) obtained using full vectorial mode solver and Gaussian fit for W = 0.5 μm, H = 0.22 μm. 27

3.3 Gaussian spreading scheme used for modeling the input FPR W_x is the (1/e) width of the Gaussian approximated guided mode in the r direction, W_w is the width of the waveguide, W_f is the width of FPR region and z_L is the distance at which the (1/e) width becomes $\sqrt{2}W_{x0}$. . . 32

3.4 (a) Calculated correction factor (α) and W_y variations (calculated from Lumerical mode Solver) as a function of tapered waveguide width W (interconnecting input waveguide and input FPR) for 2-μm-SOI AWGs; (b) Calculated correction factor (α) and W_y variations as a function of tapered waveguide width W (interconnecting input waveguide and input FPR) for 220-nm-SOI AWGs. 33

3.5 (a) Comparison of electric field amplitude along the propagation direction with and without the correction factor for 2-μm-SOI; (b) Comparison of electric field amplitude along the propagation direction with and without the correction factor for 220-nm-SOI. 34

3.6 Spreading scheme and wavelength dependent interference of Gaussian beams (emerging from the waveguide array) at the focal plane of output FPR. 36

3.7 (a) Comparison of output spectrum of 8 channel, 100 GHz AWG in 2-μm-SOI computed by RSoft BeamPROP and Gaussian approximation using α= 0.59; (b) Comparison of experimental results of 7-channel AWG in 220-nm-SOI with Gaussian approximation using α = 0.5. . 37

3.8 Crosstalk degradation as a function of waveguide width variation for AWG on 2-μm-SOI and 220-$nm-$-SOI (TE polarization). 38

3.9 (a) Spectrum of AWG on 2-μm-SOI with no variation in waveguide width; (b) Spectrum of AWG on 2-μm-SOI with probabilistic waveguide width variations of 25 nm. 39

4.1 Mask layout of designed AWG. The straight and bend waveguides are kept for reference. 42

4.2 SEM images of mask (a) straight waveguide region for which the waveguide width is found to be uniform; (b) Bend waveguide region for which the width is found to be varying. 43

4.3 Fabrication process flow. 46

4.4 Confocal microscopic image of arrayed waveguides near input FPR and output waveguides near output FPR. 46

4.5 Confocal microscopic image of arrayed waveguides near input FPR and output waveguides near output FPR. 47

4.6 Confocal microscopic image of arrayed waveguides near input FPR and output waveguides near output FPR. 47

4.7 Confocal microscopic image of arrayed waveguides near input FPR before and after the descum. 48

4.8 Confocal microscopic images of PPR patterns of fabricated AWG on SOI. 49

4.9 Confocal microscopic images of fabricated AWG on SOI after RIE. 49

4.10 SEM images of three arrayed waveguides showing the width variation in arrayed waveguides. 50

4.11 SEM images of a sample arrayed waveguide showing the lengthwise width variation. 50

4.12 Waveguide width plotted against the arrayed waveguide number. . . 51

4.13 Waveguide width plotted against the arrayed waveguide number. . . 51

5.1 Rowland circle geometry proof, D is the source and E is the point where image is assumed to be formed. 55

ABBREVIATIONS

Acronyms

AWG	Arrayed Waveguide Grating
Band C	Conventional wavelength band ($\lambda \sim 1527$ to 1567 nm)
Band L	Long wavelength band ($\lambda \sim 1567$ to 1607 nm)
BOX	Buried Oxide
BPM	Beam Propagation Method
DC	Direct Current
DI	De-ionized (water)
DWDM	Dense Wavelength Division Multiplexing
FDTD	Finite Difference Time Domain
FEM	Finite Element Method
FPR	Free Propagation Region
FSR	Free Spectral Range
ICP	Inductively Coupled Plasma
PPR	Positive Photoresist
RF	Radio Frequency
RIE	Reactive Ion Etching
SEM	Scanning Electron Microscope
SOI	Silicon-On-Insulator
TE	Transverse Electric (polarization)
TM	Transverse Magnetic (polarization)
UV	Ultra-Violet

Chemical Names

Ar	Argon
Cr	Chromium
HF	Hydro Fluoric Acid

HNO_3	Nitric Acid
H_2O	Water
NaOH	Sodium Hydroxide
SF_6	Sulfur Hexafluoride
Si	Silicon
SiO_2	Silicon dioxide
TCE	Tri-chloro Ethylene

Units

dB	Decibel
Hz	Hertz
mW	milli Watts
mT	milli Torr
μm	Micro meter
M	Molar
nm	nano meter
sccm	standard cubic centimeter per minute
mTorr	milli-Torr (of pressure)
mbar	milli-Bar (of pressure)
ml	milli-liter (of fluid)
V	Volts (of fluid)

NOTATION

$\mathbf{n}$	Refractive index
$\mathbf{n}_{eff}$	Effective refractive index
$\mathbf{E}$	Complex electric field amplitude
Ψ	Real electric field amplitude
Δ	Del operator
$\boldsymbol{\lambda}$	Wavelength
$\boldsymbol{\beta}$	Propagation constant
$\boldsymbol{\phi}$	Phase of the EM wave
$\mathbf{f}$	focal length of FPR
$\mathbf{R}$	Waveguide bending radius
$\mathbf{L}$	Length (refers to device length, component length)
$\boldsymbol{\Gamma}$	Overlap integral coefficient
$\boldsymbol{\alpha}$	Loss per unit length
$\boldsymbol{\delta_{dB}}$	Polarization extinction
$\boldsymbol{W_x}$	1/e width of electric field distribution in horizontal direction (along x-axis)
$\boldsymbol{W_y}$	1/e width of electric field distribution in vertical direction (along y-axis)
$\boldsymbol{W_0}$	Beam waist/Minimum spot size

CHAPTER 1

Introduction

1.1 Motivation

Photonic interconnects are better choice compared to conventional electrical interconnects because of their higher speed of operation and lower power dissipation (in terms of energy per bit). Over the last few years, outstanding progress has been made in the field of integrated optics, with the advancements in the CMOS-compatible fabrication techniques. Possible power savings and high speed interconnects were the driving thoughts for the growth of integrated optics. As the number of internet users increased, the demand for more data bandwidth led to revolution in the optical data links starting from early coaxial cable to multi channel WDM systems. Wavelength Division Multiplexing (WDM) is a technique used to improve the bandwidth efficiency of the channel. Multiple wavelengths carrying different signals can be transmitted simultaneously along a single communication media using this technique. Two commonly used methodologies of Wavelength Division Multiplexing are Coarse Wavelength Division Multiplexing (CWDM) and Dense Wavelength Division Multiplexing (DWDM). Channel spacing of CWDM is $\sim$ 20 - 30 nm and are commonly used in local communication networks (eg : Metro Television). DWDM signal channels are very closely spaced with channel spacing $\sim$ 0.8 - 1.6 nm and demands highly sophisticated designing and execution since the channels are densely packed. The three most commonly used techniques for MUX/DEMUX applications are ring resonators, Fiber Bragg Gratings (FBGs) and Arrayed Waveguide Gratings (AWGs). Using ultra small ring resonators [1, 2] and coupled ring with different radii [3, 4] MUX/DEMUX operation can be performed. It is possible to extend the free spectral range up to 30 nm to include more number of channels using this technique. However, ring based MUX/DEMUX has an inherent disadvantage that they are only suited for low to medium channels (4 - 8 channels) and this approach rely on high-resolution Electron Beam Lithography [EBL] [5, 6] to obtain the uniform channel spacing and becomes more complex when more number of wavelength need to be multiplexed. Nowadays, AWGs are widely used because it provides uniform channel spacing, reasonable bandwidth of passband, good extinction ratio and lower crosstalk. Moreover, AWG has an advantage of lesser price per channel with increasing the channel count. With the advancements in the CMOS fabrication techniques, it is possible to realize AWG (de-)multiplexers with very small footprint. FBGs are shown to be working well for low to medium channels (4 - 8 channels) for a channel spacing of 50 GHz or lower.

Arrayed waveguide grating (AWG) has wide-spread applications in fiber-optic dense wavelength division multiplexing systems. They have been successfully demonstrated in different platforms such as InP [7, 8, 9], SiO_2 [10, 11], Su-8 polymer [12], Si_3N_4 [13], SOI [14, 15] etc. The higher refractive index of SOI device layer and its CMOS fabrication process compatibilities allow to design AWG structures with smaller footprints [16], which may be potentially useful for on-chip optical interconnect applications. The crosstalk due to signal-noise interference in a AWG based N $\times$ N optical interconnect network has already been studied [17]. Moreover, extensive researches are going on to reduce the sidelobe [18], polarization dependency [19] and improve the crosstalk [20] etc. It has been also shown recently that the fabrication related non-uniformity and/or inhomogeneities in waveguide dimensions in an AWG, especially when fabricated in high index contrast SOI platform play a crucial role in cross-talk degradation [21]. A nanometer-scale random variation in waveguide cross-sections causes a huge phase error accumulation and subsequently, resulting into large deviations in the spectral characteristics of a SOI based AWG [22, 23]. Fabrication tolerance of integrated optic devices on SOI platform were studied extensively [24, 25]. The use of fabrication tolerant waveguides [26] and bends [27] should reduce the effect of fabrication imperfections of the arrayed waveguides. AWG layouts can also be improved to reduce the phase error [28]. E-beam lithography [29] and deep UV lithography (193-nm) [30] are most commonly used method for fabricating AWGs, since they provide a better structural uniformity. Feasibility of using i-line lithography in fabrication of AWGs on 2-μm-SOI has not been studied extensively till now. In spite of all these advancements, phase error remains as a major issue to be resolved. However, most of the recent researches on AWG does not analyze the distortion in the spectrum due to fabrication induced imperfections [31, 32, 33]. Therefore, a rugged design tool is required to analyze the device performance and to estimate fabrication tolerance of SOI based AWG structures with desired specifications. Previous attempts to analyze the performance of AWG using semi analytical methods were limited to SiO_2-Ta_2O_5 AWGs [34] and InP AWGs [35], which were designed with relatively larger waveguide geometry. The FDTD design tools are available but they demand for a huge computational budget as the effective footprint of an AWG can be $\sim 5\ mm^2$ or more. The BPM simulation is relatively faster but not suitable for compact AWGs which have sharp bends and tightly confined modes.

1.2 Research Objective

Arrayed Waveguide Gratings fabricated on high index contrast SOI substrates have very poor fabrication tolerance. Simulation and analysis of phase error of this structure using commercial simulators demand huge computation budget because of the large footprint and very small features of the device. The objective of this M.S. research work is to develop a semi-analytical method to analyze the AWG using Gaussian beam approximation of guided mode profiles which will be nearly accurate and faster compared to the commercial FDTD design tools and study the fabrication tolerance of AWGs in general especially on AWG fabricated using commonly used i-line contact lithography technique.

1.3 Thesis Organization

Chapter 2 explains the design aspects of AWG on 2-μm-SOI and 220-nm-SOI. Chapter 3 describes the Gaussian beam approximation of guided mode profiles to simulate AWG. Comparison of the spectrum of AWG using this method and commercial simulators like RSOFT BeamPROP and Lumerical (for sub micron waveguide cross sections) has been discussed. The phase error analysis of AWG on SOI with different device layer thickness (2-μm and 220-nm) is done in this chapter. In chapter 4, fabrication of AWG on 2-μm-SOI using i-line lithography has been discussed. The non uniformity in the fabricated arrayed waveguide geometry of the fabricated device has been analyzed. Finally, chapter 5 summarizes this work and explains the outlook of the entire work.

CHAPTER 2

Theory and Design

In this chapter, basic working principle and design aspects of AWGs are discussed. Effects of various parameters on the spectral characteristics of AWG are explained and an optimized design of AWG on Silicon-On-Insulator (SOI) with device layer thicknesses of 2-μm and 220-nm are discussed.

2.1 Working principle

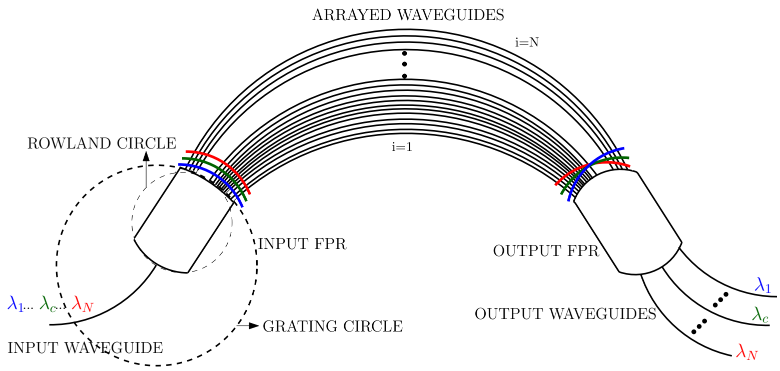

Figure 2.1: Scheme of conventional AWG. The device consists of Rowland circle geometry. The input/output waveguides are placed on the circumference of a circle (Rowland circle) which has a radius half of that of the circle (Grating circle) where the arrayed waveguides are placed.

A scheme of conventional AWG has been shown in Fig. 2.1. AWG consists of input/output waveguides, arrayed waveguides and input/output Free Propagation Regions (FPRs). The FPRs are designed based on the Rowland circle geometry. The input waveguides (arrayed waveguides) are placed on the periphery of a circle called Rowland circle (Grating circle). Radius of the Rowland circle is half of that of the Grating circle. The Rowland circle theorem says that if we have a source on the periphery of the Rowland circle, the diffracted beams from the Grating circle will make an image on the Rowland circle itself (see Appendix A). The incoming DWDM signals which are having wavelengths with very small channel spacing propagates into the input FPR. Once it enters the input FPR, the beam diverges in a similar fashion irrespective of wavelength. The light is collected by and propagates individually in the arrayed waveguides. Each of the arrayed waveguides is having a path length greater than the previous one equal to the integer multiple of the center wavelength (λ_c) in the arrayed waveguide.

$$\Delta L = \frac{m\lambda_c}{n_{eff}} \tag{2.1}$$

where m is the grating order, λ_c is the center wavelength and n_{eff} is the effective index of the arrayed waveguide. So, for the center wavelength, the wave in each arm will reach at the output FPR with the same relative phase and it makes an image at the center of the output FPR (refer Fig. 2.1). For a wavelength smaller (larger) than the center wavelength, λ_1 (λ_8) the phase front will be tilting upwards (downwards) and the focusing point will be above (below) the focusing point of the center wavelength (λ_c). At these focal points on the output FPR, output waveguides are placed to properly confine and guide out the focused fields.

2.2 Design Parameters

The complete design of an arrayed waveguide grating is explained with the help of Fig. 2.2 below [36].

Considering a general case of arrayed waveguide grating with one input and N number of outputs. The enlarged view of output FPR has been shown in Fig. 2.2. Consider two light rays passing through the i^{th} and $(i-1)^{th}$ arrayed waveguide. The input FPR will be having similar configuration with one input. f is the focal length of the FPR. The phase difference between two light rays passing through i^{th} and $(i-1)^{th}$ arrayed waveguides should be an integer multiple of 2π for those two rays to have a constructive interference at point x in the output focal plane. D_i and D_o are the separation between

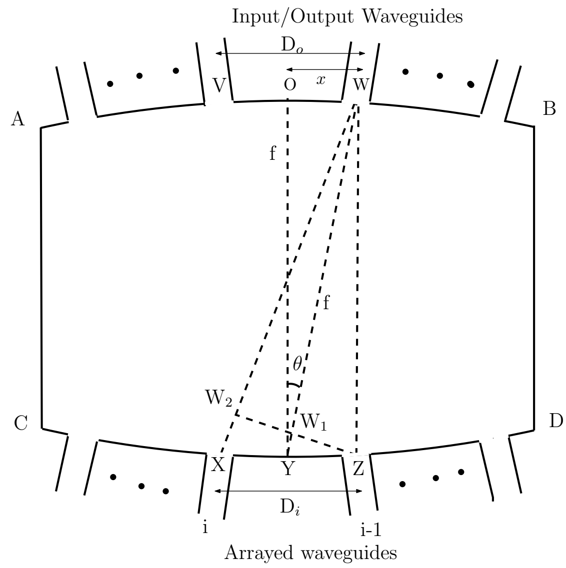

Figure 2.2: Input/output FPR model. f is the focal length of FPR, D_i is the separation between arrayed waveguides, D_o is the separation between output waveguides, i is the number of arrayed waveguide, V and W are the focusing points at the output focal plane and O is the reference point at which x = 0. It is assumed that the light from different arrayed waveguides are accumulated at a distance x from the reference point O.

neighboring arrayed waveguides and output waveguides respectively. From Fig. 2.2, $YW = YO = f$, the focal length of the ouptut FPR. Consider x as the focal point at the output focal plane, $x = f\theta$. Since $XZ = D_i$ and angle between XZ and W_2Z is θ, from the right angled triangle XW_2Z we can derive $XW_2 = D_i sin\theta$. Similar logic can be applied to right angled triangle, YW_1Z to get $YW_1 = (D_i/2)sin\theta$. Assuming f is large enough to consider $XW, YW and ZW$ to be parallel to each other we can easily derive $XW = f + (D_i/2)sin\theta$ and $ZW = f - (D_i/2)sin\theta$. Assuming the angle of dispersion θ to be very small, we can assume $sin\theta \approx \theta = x/f$. Hence, $XW = f + (D_i/2)sin\theta = f + (D_i x/2f)$ and $ZW = f - (D_i/2)sin\theta = f - (D_i x/2f)$. So, the total phase accumulated at x for a light ray passing through i^{th} arrayed waveguide

$$\Phi_i = \beta_s f + \beta_{eff}(L_c + i\Delta L) + \beta_s(f + \frac{D_i x}{2f}) \tag{2.2}$$

and the total phase accumulated at x for a light ray passing through $(i-1)^{th}$ arrayed waveguide

$$\Phi_{i-1} = \beta_s f + \beta_{eff}(L_c + (i-1)\Delta L) + \beta_s(f - \frac{D_i x}{2f}) \tag{2.3}$$

where, $\beta_s(2\pi n_s/\lambda$, n_s is the effective index of slab) and $\beta_{eff}(2\pi n_{eff}/\lambda$, n_{eff} is the effective index of the arrayed waveguide) are the propagation constants of the FPR and arrayed waveguide respectively. L_c is the smallest arrayed waveguide length, i is the arrayed waveguide number and ΔL is the incremental length between any two neighboring arrayed waveguides.

So the condition for interference at x is

$$\Phi_i - \Phi_{i-1} = 2m\pi \tag{2.4}$$

where m is an integer and substituting eqn. 2.2 and 2.3 to eqn. 2.4,

$$\beta_{eff}\Delta L + \beta_s \frac{D_i x}{f} = 2m\pi \tag{2.5}$$

Substituting $\beta_{eff} = 2\pi n_{eff}/\lambda$ and $\beta_s = 2\pi n_s/\lambda$ we get,

$$n_{eff}\Delta L + n_s \frac{D_i x}{f} = m\lambda \tag{2.6}$$

We have chosen ΔL in such a way that $\beta_{eff}\Delta L = 2m\pi$ for the center wavelength (λ_c). Hence the focusing point for the center wavelength will be at $x = 0$ at the output focal plane as per eqn. 2.6. Differentiating eqn. 2.6 with respect to the wavelength λ around the center wavelength λ_c, and substituting $m = \frac{n_{eff}\Delta L}{\lambda_c}$ we get,

$$n_s \frac{D_i}{f}\frac{dx}{d\lambda} - \frac{1}{\lambda_c} n_{eff}\Delta L + \frac{dn_{eff}}{d\lambda}\Delta L = 0 \tag{2.7}$$

Rearranging the eqn. 2.7 we get the dispersion relation for AWG, shown in eqn. 2.8

$$\frac{dx}{d\lambda} = \frac{n_g \Delta L f}{\lambda n_s D_i} \tag{2.8}$$

where n_g (n_{eff} - $\lambda \frac{dn_{eff}}{d\lambda}$) is the group index of the arrayed waveguide. Now to find the FSR, we can use eqn. 2.6. For a frequency $\nu + FSR$, let the change in arrayed waveguide refractive index (n_{eff}) be Δn_{eff} and the effective index of slab region is independent of the frequency within the FSR region of frequencies. So, the interference condition for frequency $\nu + FSR$ for the order $m + 1$ is given by,

$$n_s \frac{D_i x}{f} + (n_{eff} + \Delta n_{eff})\Delta L = (m+1)\frac{c}{\nu + FSR} \tag{2.9}$$

where,

$$\Delta n_{eff} = \frac{dn_{eff}}{d\nu} FSR = \frac{dn_{eff}}{d\lambda} \frac{-c}{\nu^2} FSR \tag{2.10}$$

Substituting eqn. 2.10 in 2.9 and subtracting eqn. 2.6 from it with the approximation $\nu(\nu + FSR) \approx \nu^2$, we get

$$FSR = \frac{c}{n_g \Delta L} \tag{2.11}$$

in terms of frequency and in terms of wavelength,

$$FSR = \frac{\lambda_c n_{eff}}{m n_g} \tag{2.12}$$

These are the basic equations used for designing AWGs.

$$FSR = \frac{\lambda_c n_{eff}}{m n_g} = N_{chan} \Delta\lambda \tag{2.13}$$

where, FSR is the free spectral range, λ_c is the center wavelength of operation, n_{eff} is the effective index of the waveguide, n_g is the group index of the waveguide, m is the grating order, N_{chan} is the number of output channels, $\Delta\lambda$ is the channel spacing. The only unknown, the grating order m can be found from eqn. 2.13. Using eqn. 2.14, the length increment of the arrayed waveguides region, ΔL can be found.

$$\Delta L = \frac{m\lambda_c}{n_{eff}} \tag{2.14}$$

The only remaining unknown parameter, the focal length of FPR (f) can be found by modifying eqn. 2.7 as given below.

$$f = \frac{D_i D_o n_s n_{eff}}{m \Delta\lambda n_g} \tag{2.15}$$

where, Di (D_o) is the separation between input (output) waveguides of FPR, n_s is the effective index of the slab region.

Commercially procured SOI wafer has various standard device layer thickness. 220-nm device layer SOI wafers are used to make very compact devices for on-chip optical interconnect applications with CMOS-compatible fabrication techniques, but the device is found to have higher polarization dependency and waveguide dispersion. In applications like integrated photonic micro-spectrographs [37], where the fiber has been directly connected to the AWG on chip, 2-μm device layer thickness is preferred to minimize the coupling loss. The importance of waveguides fabricated on 2-μm-SOI comes in this context. So, the recent trend is to design interconnect devices with relatively large waveguide cross-section devices (2-3 μm) [38, 39]. However, the advantages of single mode guiding properties and polarization independencies in such larger waveguide cross-section waveguides are not fully exploited.

2.3 Design with 2-μm-SOI

Commercially used DWDM channel spacings are 0.8 nm (100 GHz) and 0.4 nm (50 GHz). Most of the DWDM system presently uses 100 GHz channel spacing. Design of an 8 channel 100 GHz AWG on 2-μm-SOI has been explained in this chapter. Optimization of various structural parameters such as waveguide width (W), waveguide height (H), slab height (h), separation between arrayed waveguides (D_i), number of arrayed waveguides required, separation between output waveguides (D_o) and minimum bend radius that can be used is discussed below.

2.3.1 Single Mode Waveguide

Single mode waveguide is the fundamental building block of any integrated optoelectronic device. Fig. 2.3 shows scheme of a rib waveguide on SOI platform. Here, air and buried oxide layer (BOX) act as the cladding and the confinement along the vertical direction is provided by the total internal reflection at the top (Silicon-air) and bottom (Silicon-BOX) boundaries. The difference in height between rib height (H) and slab height (h) provides the horizontal confinement of the field. One needs to carefully choose waveguide width (W), rib height (H) and slab height (h), so that the geometry supports only single mode of operation for both TE and TM polarization.

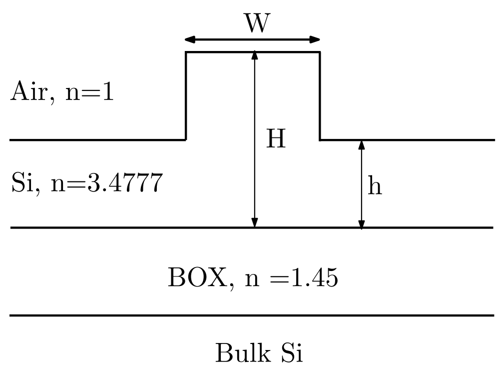

Figure 2.3: Schematic cross-section view of SOI rib waveguide, W is the rib height, H is the rib height and h is the slab height. W, H and h can be carefully chosen to ensure single mode guiding.

RSOFT - FEMSIM has been used in order to estimate the waveguide width (W) and slab height (h), which ensure single mode guiding at around λ = 1550 nm. The slab height (h) has been fixed to be 1 μm to obtain a strong horizontal confinement of the mode. This is very essential as there are lot of bend waveguides with very small bend radii. Now keeping H = 2 μm and h = 1 μm, effective index of both fundamental and first order mode for TE and TM polarization have been monitored by varying W. A rib waveguide becomes multimoded when the first order mode effective index becomes greater than the effective index of the slab waveguide (for a particular polarization). In Fig. 2.4, N_0^{TE} (N_0^{TM}) and N_1^{TE} (N_1^{TM}) represent the fundamental and first order mode effective indices of TE (TM) polarization. For TE polarization, N_1^{TE} at W $\sim$ 2 μm, becomes larger than slab effective index, which means for W > 2 μm the first order mode starts guiding and the waveguide becomes muti-moded for TE polarization. Similarly, for TM polarization, for W > 1.6 μm the waveguide becomes multi-moded. In order to ensure single mode operation around 1550 nm for both TE and TM polarizations, the waveguide width W should be less than 1.6 μm.

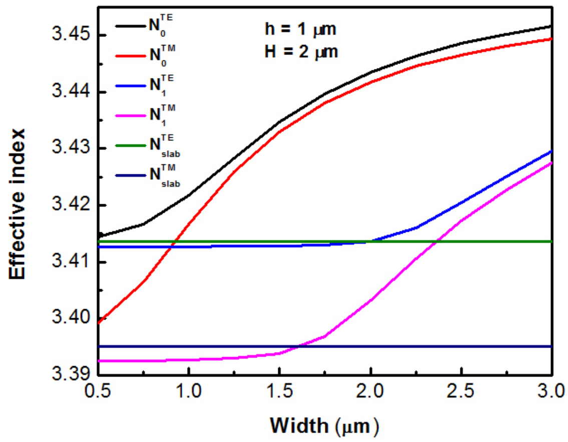

Figure 2.4: Waveguide dispersion relation for extracting waveguide parameters for single mode operation of 2-μm-SOI. For W > 1.6 μm the effective index of first order modes are greater than the slab modes and hence the waveguide will be multimoded.

Conventional AWG device (Fig. 2.1) consists of lot of bend waveguides of different bend radii and hence it is necessary to design a waveguide geometry which provides good confinement of mode. Fig. 2.5 compares mode profiles of two waveguides of width 1 μm and 1.5 μm respectively, keeping h = 1 μm and H = 2 μm. As we reduce the waveguide width, we are reducing the effective index of the core region and thereby the index contrast between the core and the slab regions. As we see from Fig. 2.5, the mode becomes less confined when waveguide width is 1 μm. Hence W has been chosen to be 1.5 μm.

2.3.2 Input FPR

Optimization of separation between Arrayed Waveguides ***(D_i)*** : Separation between arrayed waveguides (D_i) at input FPR - arrayed waveguide junction and output FPR -

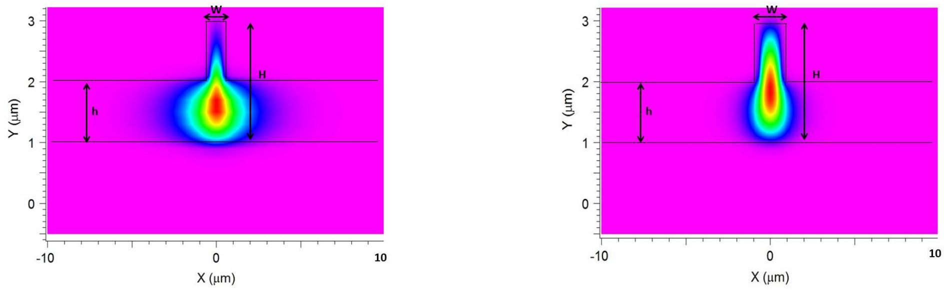

(a) (b)

Figure 2.5: Simulated mode profiles of the rib waveguide fo H = 2 μm, h = 1 μm (a) W = 1 μm (b) W = 1.5 μm.

arrayed waveguide junction is very crucial because of the following reasons.

1. Loss : As we increase the separation between arrayed waveguides, keeping the arrayed waveguide width constant, more light gets radiated through the gap and the loss at the input FPR - arrayed waveguides junction increases.

2. Phase error due to coupling : As we reduce the separation between arrayed waveguides, there will be unwanted coupling between them which will account for phase errors.

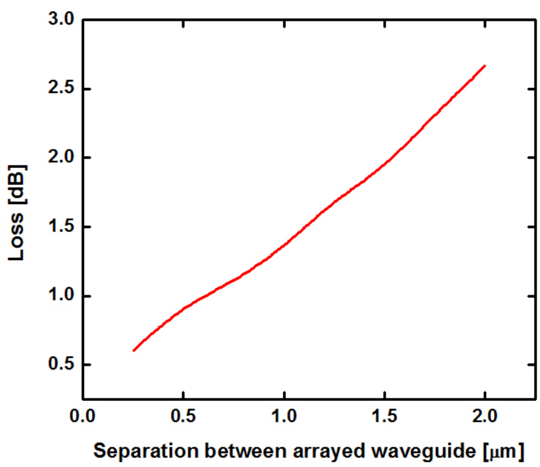

Figure 2.6: Theoretical junction loss at input FPR - arrayed waveguide junction as a function of separation between arrayed waveguides (D_i).

Hence it is important to find a trade off between loss and phase error. For device fabricated on 2-μm-SOI, a value of 1 μm will be sufficient to minimize the coupling between arrayed waveguides near FPR - arrayed waveguide junction for the designed waveguide parameters (W = 1.5 μm, H = 2 μm, h = 1 μm). Due to the diffraction effects during the lithographic process, a slight increment in the separation between arrayed waveguides is expected. So the loss at the input FPR - arrayed waveguide junction as a function of separation between arrayed waveguides was studied and the result has been shown in Fig. 2.6. When the separation between arrayed waveguide increases from 1 μm to 2 μm, an increment in loss of nearly 1 dB is expected.

Optimization of number of arrayed waveguides : The light diverging from the input waveguide at the input FPR, should be collected efficiently without much loss using large number of arrayed waveguides. However, increasing the number of arrayed waveguides will ultimately result in larger footprint of the device. S. Pathak et. al [30], explains a rule of thumb that can be used to decide the number of arrayed waveguides.

$$N = 3.5\frac{FSR}{\Delta\lambda} \tag{2.16}$$

where, N is the number of arrayed waveguides, $\Delta\lambda$ is the channel spacing and FSR is estimated using eqn. 2.13. So in our case, for an 8 channel, 100 GHz AWG, number of arrayed waveguides required is 28.

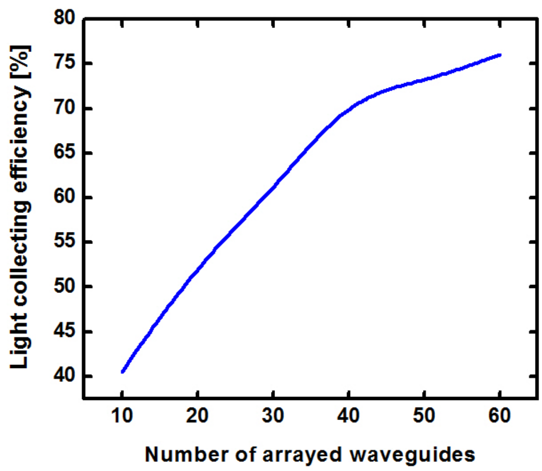

Figure 2.7: Light collection efficiency of the arrayed waveguides at the inpt FPR - arrayed waveguide junction as a function of number of arrayed waveguides (N).

However, as mentioned earlier, the light collection efficiency at the input FPR - arrayed waveguide junction is a major factor in determining the number of arrayed waveguides, which is defined as,

$$\text{Light collection efficiency} = \frac{\sum_{i=1}^{N} P_i}{P_L} \tag{2.17}$$

where, N is the total number of arrayed waveguides, P_i is the power coupled to i^{th} arrayed waveguide and P_L is the launch power. For a 2-μm-SOI AWG, keeping the separation between arrayed waveguide as 1 μm (as discussed in section 2.3.1), we plotted the light collection efficiency as a function of number of arrayed waveguides. Using 28 numbers of arrayed waveguides as explained by the thumb rule, the light collection efficiency is found to be only 60 $\%$ as shown in Fig. 2.7. The light collection efficiency almost saturates at nearly 75 $\%$ as we increase the number of arrayed waveguides above 40. When there is an increase in the number of arrayed waveguides there is an effective increase in the FPR width only. FPR length remains constant since it is independent of number of arrayed waveguides. Hence the light collected by outermost arrayed waveguide is minimal and the light collecting efficiency does not improve beyond a point. It has been found that increasing the number of arrayed waveguides beyond 40 will not yield any additional benefit, but will increase the footprint of the device. So for the AWG on 2-μm-SOI the number of arrayed waveguides has been chosen to be 40.

2.3.3 Output FPR

Optimization of separation between output waveguides (D_o) :

Separation between output waveguides (D_o) can be increased to ensure sufficiently low crosstalk between two neighboring channels. From eqn. 2.15 we know that as separation (D_o) between output waveguide increases, the focal length of FPR and the total footprint of the device increases.

From Fig. 2.8 one can conclude that a separation of 3 μm between output waveguides, improves the crosstalk to a value less than -30 dB for an AWG on 2-μm-SOI.

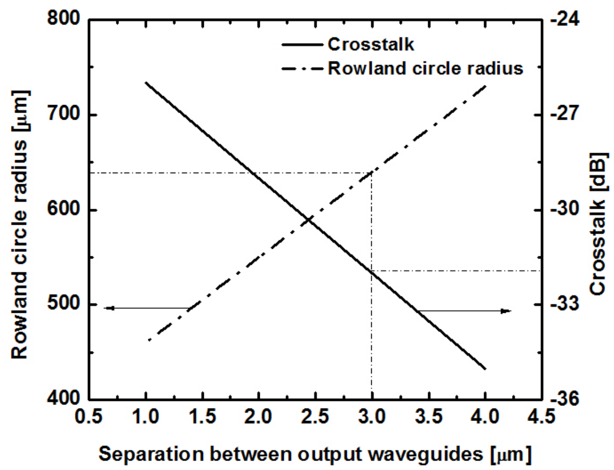

Figure 2.8: Crosstalk and Rowland circle radius as a function of output waveguide separation (D_o) for AWG fabricated on 2-μm-SOI. A separation value of 3 μm gives a crosstalk $\sim$ -32 dB.

2.3.4 Arrayed waveguides

Optimization of bending radius : Bend waveguides are incorporated in AWGs, with different bend radii to provide the required path length difference (ΔL) between two neighboring arrayed waveguides. It is important to determine the minimum bend radius that can be used which will ensure minimal bend loss. The bend loss as a function of bend radius is analyzed in this section.

A typical 90^0 waveguide consists of two straight sections (AB and CD) and a bend section (BC) as shown in Fig. 2.9. Mode profiles of a straight and bend waveguides are compared in Fig. 2.10.

The guided mode in bend waveguide region will be shifted towards the outer side of the bend and will be different to the guided mode in straight waveguide region due to the bend induced effective index change. This shift or change in the mode profile give rise to two types of losses in the bend waveguides.

Total loss in a 90^0 bend can be divided into two.

1. Transition loss : At the junctions B and C in Fig. 2.9, due to the mode mismatch between modes of straight and bend region, there will be a transition loss. As we reduce the bend radius, the bend induced refractive index change will be high and the transition

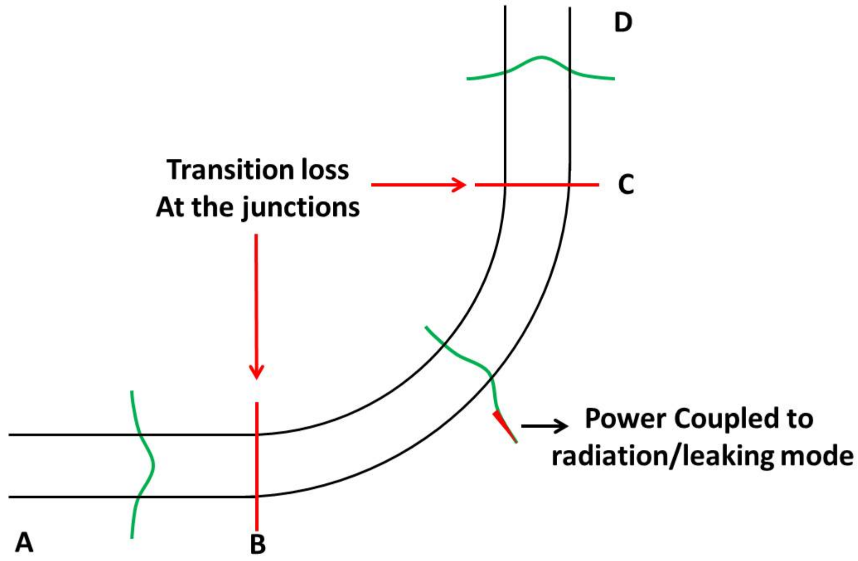

Figure 2.9: Schematic representation of losses in a 90^0 bend.

loss also will be high.

2. Radiation loss : As mentioned earlier when the mode shifts more toward the outer side of the bend region there is a higher probability that coupling to the higher order radiating modes can happen. Since the waveguide geometry supports the single mode guiding, the light that is getting coupled to the higher order modes gets radiated. For bend waveguide of smaller bend radius the mode shift is more and there is a higher probability of light getting coupled to the higher order radiating modes. The imaginary part of the refractive index of the bend region gives us the radiation loss.

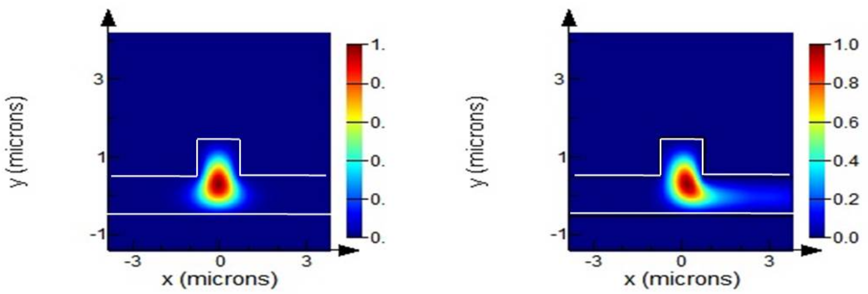

Figure 2.10: Calculated mode profiles of a straight and a 90^0 bend waveguide (radius 100 μm) on 2-μm-SOI using Lumerical mode solver.

The total loss due to a 90^0 bend is the sum of transition loss that is happening at the two boundaries and the radiation loss.

Lumerical full vectorial mode solver (2015b) has been used to solve for the modes and effective indices of bend and straight waveguides (see Fig. 2.10). The overlap integral between these two modes will give us the transition loss. The imaginary part of effective index of the bend region will give the radiation loss. Hence,

The total loss due to a 90^0 bend = $2\times$Transition loss + Radiation loss

The estimated total loss due to a 90^0 bend for different bend radii for both TE and TM polarization for a waveguide on 2-μm-SOI, which is plotted in Fig. 2.11.

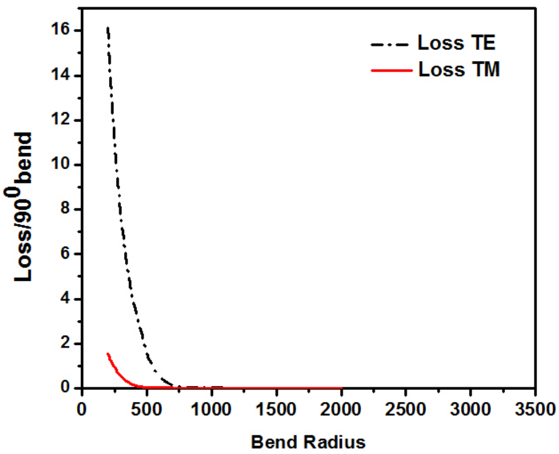

Figure 2.11: Bend loss of a 90^0 bend for different bend radii for waveguides on 2-μm-SOI. For a particular bend radius, loss for TM polarization is less compared to TE polarization.

For a given bend radius, the radiation loss and the transition loss are low for TM mode compared to the TE mode. This is because, TM mode is more confined in the waveguide core region because of its higher index contrast compared to the TE mode. Hence, the light that gets coupled higher order radiating mode is less for TM mode compared to TE mode. From Fig. 2.11, we can see that the loss increases rapidly for bend radius less than 750 μm. Hence the minimum bend radius was chosen to be 1000 μm for the arrayed waveguides.

2.3.5 Optimized design parameters

Various design aspects of AWG are discussed till now. RSOFT AWG design package is used to design the AWG with the optimum design parameters, which are shown in Table

2.1(TE polarization). For TM polarization, the effective index of the arrayed waveguide is found to be 3.441. So for TM polarization we expect a lateral shift of approximately 0.38 nm.

Two ways of designing AWGs are possible. One with fixed bend radius for all the arrayed waveguides and the second one with different bend radii for different arrayed waveguides. In the first case, the path length difference required between any two arrayed waveguides should be incorporated mainly in the straight waveguide regions, because the bend radii are fixed. In the second case, ΔL can be introduced mainly in the bend region since we have the flexibility of choosing the bend radii. Obviously, the second design is more compact compared to the first design. The minimum bend radius that has been used for designing AWG on 2-μm-SOI is 1000 μm and the total foot print of the device was found to be 1.7 $cm \times$ 0.75 cm.

Table 2.1: Optimized design parameters of AWG on 2-μm-SOI.

Parameter	Value
Number of channels	8
Channel spacing	100 GHz (0.8 nm)
Effective index of arrayed waveguide (n_a)	3.441
Slab effective index (n_s)	3.623
Grating order (m)	242
ΔL	108.9 μm
Number of arrayed waveguides	40
Separation between arrayed waveguides near FPR (D_i)	1 μm
Separation between output waveguides near FPR (D_o)	3 μm
Rowland circle diameter	594 μm
Smallest bend radius used	1000 μm
Total footprint of the device	1.7 $cm \times$ 0.75 cm

The designed AWG is simulated using RSOFT - BeamPROP. The simulation results are shown in Fig. 2.12. Different colors in the simulation results represent different channels. The simulation gives a loss of nearly 2 dB near the central wavelength (1.55 μm) mainly because of the loss in the 1 μm separation between arrayed waveguides near the input FPR region and the diffraction loss at the output FPR. The light diffracted towards the outermost channels (1.5496 μm and 1.5532 μm) are less compared to the central channels (around 1.55 μm). So there will be a non uniformity in the transmission loss for outermost channels of AWG. The channel non uniformity for the proposed AWG design is around 2 dB.

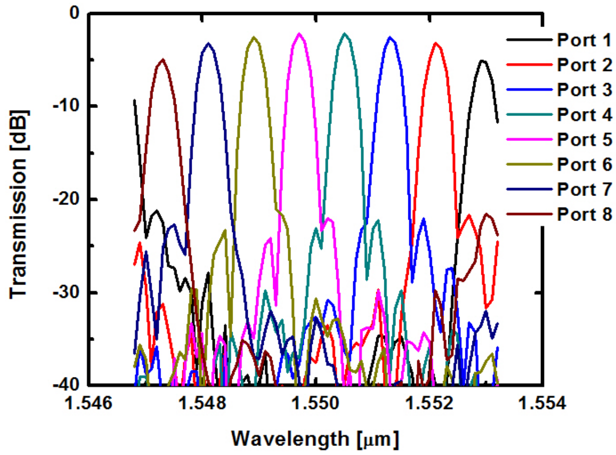

Figure 2.12: 3D simulation result of the designed AWG for the parameters shown in Table 2.1 using Rsoft-BeamPROP.

2.4 Design with 220-nm-SOI

AWG fabricated on 2-μm-SOI has some specific application as explained in section 2.3. But for on-chip applications, AWG fabricated on 2-μm-SOI is not useful due to the larger footprint of the device. Devices fabricated on 220-nm-SOI are very compact and used in on-chip optical interconnect applications. A design has been carried out for AWG on 220-nm-SOI, similar to the design of AWG on 2-μm-SOI as explained in 2.3.

2.4.1 Single Mode waveguide

Lumerical Mode Solver has been used for determining the waveguide parameters of 220-nm-SOI waveguides. The slab height (h) is assumed to be zero to ensure strong confinement of the mode. This will help to design very compact bends and thereby reduce the total footprint of the device. From Fig. 2.13, when width of the waveguide, W $>$ 0.9 μm first order TM mode effective index (N_0^{TM}) becomes greater than slab effective index (N_{slab} = 1.45) and the mode starts guiding. Similarly for TE mode, the cut off width is found to be 0.58 μm. So the width has been decided to be 0.5 μm, to ensure single mode guiding for both TE and TM polarizations.

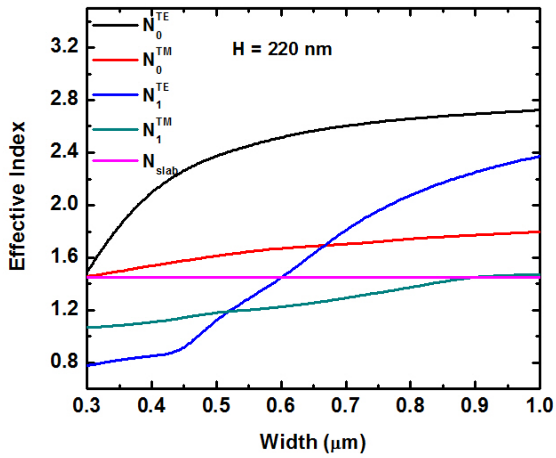

Figure 2.13: Waveguide dispersion relation for extracting waveguide parameters for single mode operation of 220-nm-SOI.

2.4.2 Input FPR

Optimization of separation between Arrayed Waveguides **(D_i) :**

For an AWG on 220-nm-SOI, since the mode is tightly confined in the waveguide, a separation of nearly 50 nm between arrayed waveguides will be sufficient to avoid the coupling between two arrayed waveguides. The loss at the junction due to a separation of 50 nm is found to be around 1.8 dB.

The loss due to fabrication imperfections at the junction has been studied and plotted in Fig. 2.14. If the separation widens to 100 nm, the loss increases to 2.75 dB.

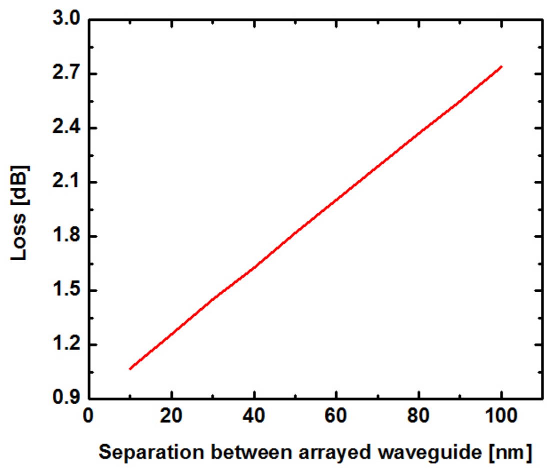

Figure 2.14: Theoretical junction loss at input FPR - arrayed waveguide junction as a function of separation between arrayed waveguides (D_i).

Optimization of number of arrayed waveguides : For AWG on 220-nm-SOI, keeping the separation between arrayed waveguides as 50 nm, the light collection efficiency has been calculated by varying the number of arrayed waveguide. When the number of arrayed waveguides are more than 20, the light collection efficiency almost saturates at 70 $\%$. But considering the rule of thumb as in eqn. 2.16, the minimum number of arrayed waveguide required has been kept as 28.

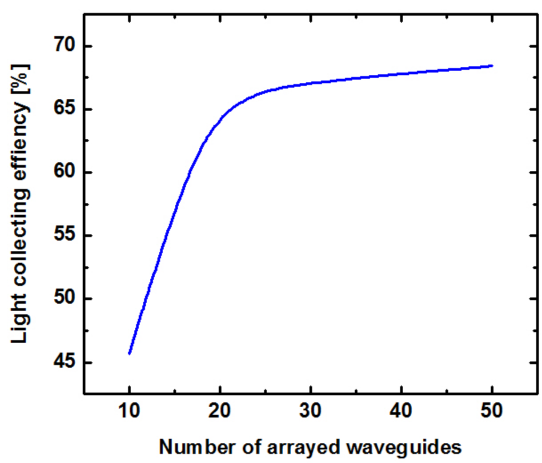

Figure 2.15: Light collection efficiency of the arrayed waveguides at the inpt FPR - arrayed waveguide junction as a function of number of arrayed waveguides (N).

2.4.3 Output FPR

***Optimization of separation between output waveguides** (D_o)* : For an AWG on 220-nm-SOI, increasing the separation between output waveguides will improve the crosstalk. However the increase in D_o will increase the FPR area and thereby the entire footprint of the device. Increasing the value of D_o from 100 nm to 500 nm improves the crosstalk by 5 dB as shown in Fig. 2.16. But in order to reduce the total footprint of the device, the separation has been fixed to be 300 nm. For this particular separation between arrayed arrayed waveguide the crosstalk is found to be around -28 dB.

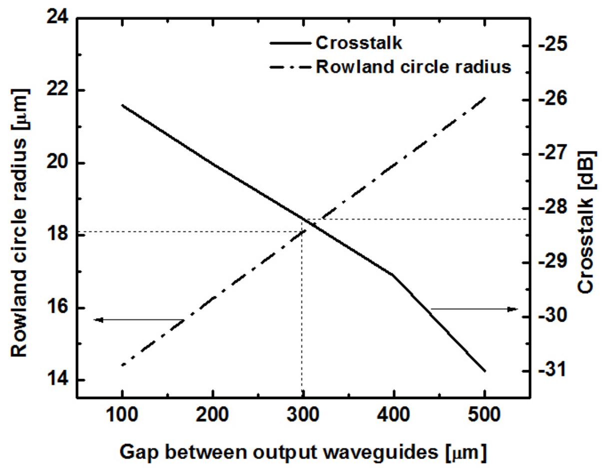

Figure 2.16: Crosstalk and Rowland circle radius as a function of output waveguide separation (D_o) for AWG fabricated on 220-nm-SOI. A separation value of 300 nm gives a crosstalk $\sim$ -28 dB.

2.4.4 Arrayed waveguides

Optimization of bending radius : Similar to AWG on 2-μm-SOI waveguides, bend loss has been calculated for AWG on 220-nm-SOI for TE and TM polarization.

Unlike waveguides on 2-μm-SOI, the confinement is very high in this case and very compact bends can be used for designing of AWG. From Fig. 2.17, a bend radius of 10 μm can be used for making compact bends. Also the confinement of the mode for TE polarization is higher compared to TM polarization and hence the loss is small for TE polarization compared to TM polarization for a given bend radius.

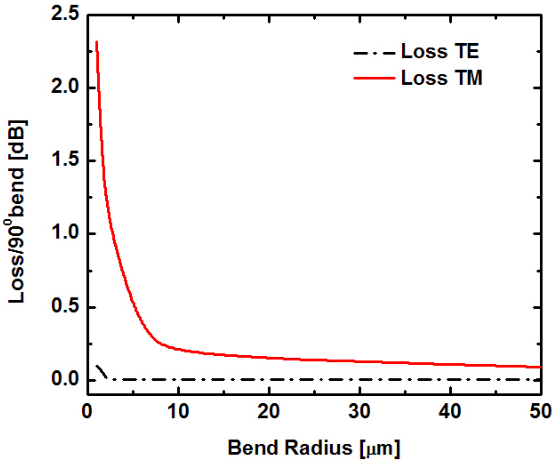

Figure 2.17: Bend loss of a 90^0 bend for different bend radii for waveguides on 220-nm-SOI. For a particular bend radius, loss for TE polarization is less compared to TM polarization.

2.4.5 Optimized design parameters

For AWG fabricated on 220-nm-SOI, we adopted a horse shoe structure [40], which gives the minimum possible footprint. The approximate area calculated is found to be 0.79 mm × 0.78 mm.

The effective index of arrayed waveguides for TM polarization on 220-nm-SOI is found to be 1.589. This will create a lateral shift of approximately 0.517 μm which explains that the devices fabricated on 220-nm-SOI waveguides are highly polarization dependent. The complete optimized parameters for TE polarization of AWG designed on 220-nm-SOI has been given in Table 2.2.

2.5 Summary

The complete design parameters of AWG on 2-μm SOI and 220-nm-SOI has been optimized. Free propagation Region of AWG designed on 2-μm-SOI can be simulated with RSOFT-BeamPROP. The addition in phase due to arrayed waveguides should be analytically incorporated before simulating the output FPR. AWG designed on 220-nm-SOI can not be simulated using RSOFT BeamPROP, since the waveguides are high contrast

Table 2.2: Optimized design parameters of AWG on 220-nmSOI.

Parameter	Value
Number of channels	8
Channel spacing	100 GHz (0.8 nm)
Effective index of arrayed waveguide (n_a)	2.386
Group Index (n_g)	4.417
Grating order (m)	131
ΔL	85.09 μm
Number of arrayed waveguides	28
Separation between arrayed waveguides near FPR (D_i)	50 nm
Separation between output waveguides near FPR (D_o)	300 nm
Rowland circle diameter	3.28 μm
Smallest bend radius used	10 μm
Total footprint of the device	0.79 mm $\times$ 0.78 mm

in nature and there are sharp bends for the structure. Only option is to go for 3D FDTD, which takes approximately 75 hours to simulate the structure. Moreover the phase error analysis due to fabrication imperfections remains a major concern for AWG designers. Because of its large footprint and very small features, numerical computations may not be appropriate for simulating a structure like AWG. Hence, it is important to develop an analytic method for simulating AWG which will be accurate and faster compared to existing numerical methods.

CHAPTER 3

Modeling and Phase Error Analysis

AWG is very sensitive to fabrication related phase errors. A nanometer-scale random variation in waveguide cross-sections causes a huge phase error accumulation and subsequently, resulting into large deviations in the spectral characteristics of a SOI based AWG. Therefore, a rugged design tool is required to analyze the device performance and to estimate fabrication tolerance of SOI based AWG structures with desired specifications. The FDTD design tools are available but they demand for a huge computational budget as the effective footprint of an AWG can be $\sim 5\ mm^2$ or more. The BPM simulation is relatively faster but not suitable for compact AWGs which have sharp bends and tightly confined modes.

In this chapter, a semi-analytical model using Gaussian beam approximation is used for the guided mode to analyze the output spectrum of AWG. Previous attempts to analyze the performance of AWG using Gaussian beam approximation were limited to SiO_2-Ta_2O_5 AWGs [34] and InP AWGs [35], which were designed with relatively larger waveguide geometry. Gaussian approximation method has also been used in modeling of flat top AWGs using Multi Mode Interference (MMI) couplers [41]. The present model uses Gaussian beam approximations for fundamental guided modes in rib waveguides and free propagation regions of the SOI based AWGs. The performance characteristics calculated by our model have been found to be in close agreement with the results obtained by commercial design tools and with published experimental results of AWGs demonstrated with photonic wire waveguides in SOI platform.

3.1 Modeling

A typical AWG consists of input/output waveguides, input/output free propagation regions (FPRs) and an array of waveguides in between (as shown in Fig. 3.1). The

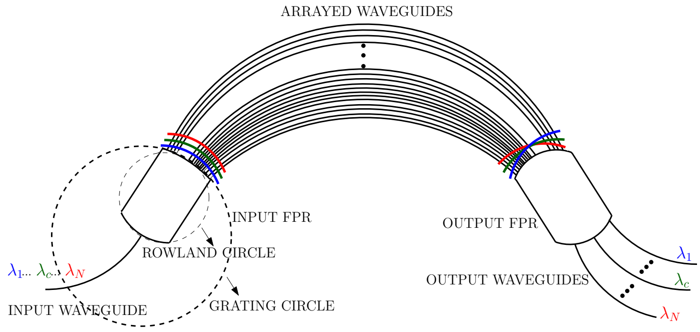

Figure 3.1: Scheme of the AWG used for modeling: three different colours are used for representing the phase-fronts of three channels $\lambda_1, \lambda_c, \lambda_N$; FPR - free propagation region.

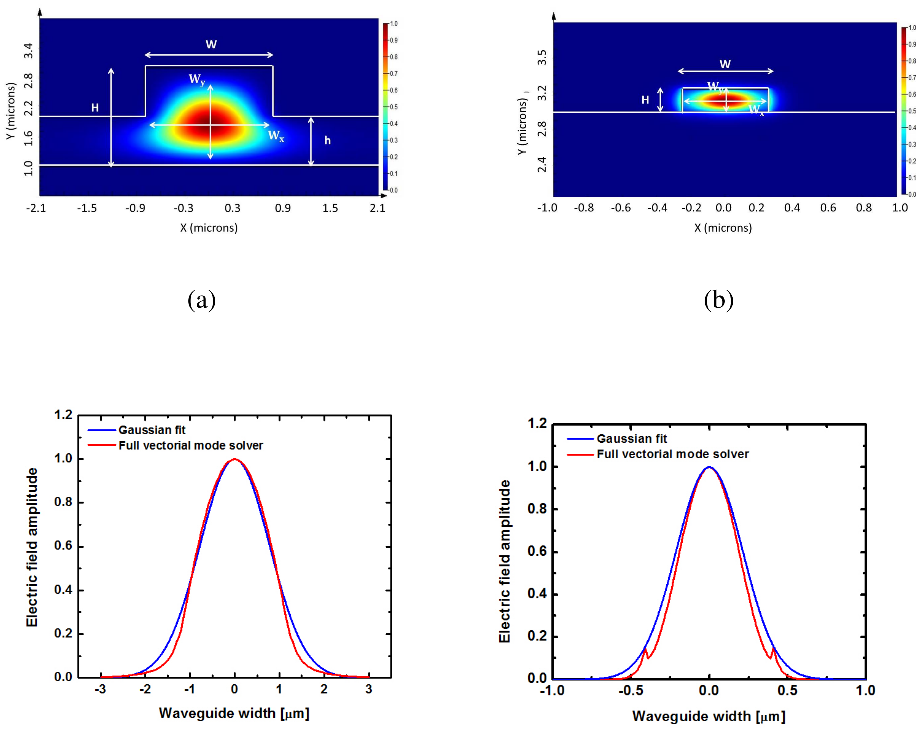

(a) (b)

(c) (d)

Figure 3.2: (a) Mode profile of a rib waveguide (TE polarization) with W = 1.6 μm, H = 2 μm, h = 1 μm; (b) Mode profile of a photonic wire waveguide (TE polarization) with W = 0.5 μm, H = 0.22 μm; (c) Comparison of 1D mode profiles of rib waveguide (TE polarization) obtained using full vectorial mode solver and Gaussian fit for W = 1.6 μm, H = 2 μm, h = 1 μm; (d) Comparison of 1D mode profiles of photonic wire waveguide (TE polarization) obtained using full vectorial mode solver and Gaussian fit for W = 0.5 μm, H = 0.22 μm.

FPR region is highly fabrication tolerant because of its larger dimension. However, a minute fabrication induced non-uniformity in the arrayed waveguides can degrade the device performance. The mode profiles (TE polarization) of single-mode waveguides (input, output and arrayed waveguides) and their corresponding effective indices are calculated using full vectorial mode solver for two different single-mode waveguide cross-sections: Fig. 3.2(a) is for $2-\mu m$-SOI (W=1.6 μm, slab height h = 1 μm) and Fig. 3.2(b) for 220-nm-SOI waveguides (W=500 nm, slab height h = 0), respectively. The computed mode profile has been used to generate 1D Gaussian field distributions with a beam waist W_x as shown in Figs. 3.2(c) and 3.2(d) for both types of waveguides. The Gaussian field is allowed to propagate freely in the input FPR and subsequently used to extract field strength and phase information for the inputs of all arrayed waveguides. Similarly, guided mode profiles and phases accumulated individually by N arrayed waveguides can be modeled into N guassian field distributions, which are then assumed to propagate in the output FPR. The superposition of these Gaussian beams are then used for taking overlap with the actual mode profiles of individual output waveguides.

The Gaussian mode profile used in the AWG analysis has been derived from the Maxwell's equations.

The Helmholtz's wave equation for the electric field can be written as:

$$(\Delta^2 + k^2)E(x, y, z) = 0 \tag{3.1}$$

where E(x,y,z) is the complex field amplitude of the vector electric field. Assuming the propagation direction to be z, we can write,

$$E(x, y, z) = \Psi(x, y, z)e^{-ikz} \tag{3.2}$$

where $\Psi(x, y, z)$ represents its variation in the transverse direction and propagation direction. Taking second order space derivative of eqn. 3.2, we get

$$\Delta^2 E = (\Delta^2\Psi)e^{-ikz} - 2ik(\Delta\Psi).e^{-ikz}a_z - k^2\Psi e^{-ikz} \tag{3.3}$$

substituting eqn. 3.2 into eqn. 3.3 and using eqn. 3.1 we get,

$$(\Delta^2 + k^2)E(x, y, z) = (\Delta^2\Psi - 2ik\frac{\delta\psi}{\delta z})e^{-ikz} = 0 \tag{3.4}$$

For further analysis, we assume

$$|\frac{\delta^2\Psi}{\delta z^2}| << 2k|\frac{\delta\Psi}{\delta z}| \tag{3.5}$$

which means that the variation of field in the propagation direction is slow on the scale of λ and

$$|\frac{\delta^2\Psi}{\delta z^2}| << |\frac{\delta^2\Psi}{\delta x^2}|, |\frac{\delta^2\Psi}{\delta y^2}| \tag{3.6}$$

which means that the variation of field in the propagation direction is slow compared to the variations in the transverse direction. Therefore, the Helmholtz equation can be written as,

$$\frac{\delta^2\Psi}{\delta x^2} + \frac{\delta^2\Psi}{\delta y^2} - 2ik\frac{\delta\Psi}{\delta z} = 0 \tag{3.7}$$

which is known as the paraxial wave equation. Assuming the solution to be cylindrically symmetric, we solve the eqn. 3.7 in cylindrical coordinates. Converting eqn. 3.7 into cylindrical coordinates,

$$\frac{1}{r}\frac{\delta}{\delta r}(r\frac{\delta\Psi}{\delta r}) - 2ik\frac{\delta\Psi}{\delta z} = 0 \tag{3.8}$$

Assuming that the solution to the paraxial wave equation is of the form,

$$\Psi(r, z) = \Psi_0 e^{-i[b(z) + \frac{kr^2}{2q(z)}]} \tag{3.9}$$

where, the subscript 0 indicates the fundamental Gaussian mode and b(z) and q(z) are two arbitrary z dependent parameters of the paraxial wave equation. Plugging this solution into the paraxial wave equation,

$$-2ik\frac{\delta\Psi_0}{\delta z} = \Big(-2k\frac{db(z)}{dz} + i\frac{k^2r^2}{q^2(z)}\frac{dq(z)}{dz}\Big)\Psi_0 \tag{3.10}$$

$$\frac{1}{r}\frac{\delta}{\delta r}(r\frac{\delta\Psi_0}{\delta r}) = \Big(-\frac{k^2r^2}{q^2(z)} - i\frac{2k}{q(z)}\Big)\Psi_0 \tag{3.11}$$

Substituting eqn. 3.10 and 3.11 into eqn. 3.8, we get

$$\frac{k^2}{q^2(z)}[\frac{dq(z)}{dz} - 1]r^2 - 2k\Big[\frac{db(z)}{dz} + \frac{i}{q(z)}\Big] = 0 \tag{3.12}$$

Equating coefficient of r^2 and constant term to zero we get,

$$\frac{dq(z)}{dz} = 1 \tag{3.13}$$

$$\frac{db(z)}{dz} = \frac{-i}{q(z)} \tag{3.14}$$

The solution to the eqn. 3.13 is $q(z) = q_0 + z$, where q_0 is the value of $q(z)$ at $z = 0$. But, if q(z) is real, we will be having zero variation in the amplitude of Gaussian beam in the r direction. So, q(z) has to be complex (z is always real). But any real value of q_0 corresponds to only spatial shift in the z axis. So, q_0 can very well be considered as an imaginary number. So, we have

$$q(z) = z + iz_R \tag{3.15}$$

$$\frac{1}{q(z)} = \frac{1}{z + iz_R} = \frac{z}{z^2 + {z_R}^2} - i\frac{z_R}{z^2 + {z_R}^2} \tag{3.16}$$

Now solving eqn. 3.13, we get

$$\Psi_0 = e^{\left(-\frac{kz_R r^2}{2(z^2+(z_R)^2)}\right)} e^{\left(-i\frac{kzr^2}{2(z^2+(z_R)^2)}\right)} e^{-ib(z)} \tag{3.17}$$

Now, solving for b(z) from eqn. 3.14, we get

$$\frac{db(z)}{dz} = \frac{-i}{q(z)} = \frac{-i}{z+z_R} \tag{3.18}$$

Integrating both sides of eqn. 3.18 from 0 to z, we get

$$ib(z) = ln(1 - i\frac{z}{z_R}) \tag{3.19}$$

Therefore,

$$e^{-ib(z)} = \frac{1}{1 - i\frac{z}{z_R}} \tag{3.20}$$

Representing this complex number in magnitude phase form, we get,

$$e^{(-ib(z))} = \frac{1}{\sqrt{1+(\frac{z}{z_R})^2}} e^{-\frac{kz_R r^2}{2(z^2+z_R^2)}} \tag{3.21}$$

Substituting eqn. 3.21 in 3.17 we can find the fundamental mode Gaussian beam as

$$E(x,y,z) = E_0 \frac{w_0}{w(z)} e^{-\frac{r^2}{w^2(z)}} e^{-i\frac{kr^2}{2R(z)}} e^{-i(k(z)-\Phi(z))} \tag{3.22}$$

where, w_0 is called the beam waist (minimum spot size)

$$w_0 = \sqrt{\frac{2z_R}{k}} \tag{3.23}$$

w(z) is the spot size of the beam at any z

$$w(z) = w_0\sqrt{1+\left(\frac{z}{z_R}\right)^2} \tag{3.24}$$

R(z) is the radius of curvature of the beam,

$$R(z) = z(1 + (\frac{z}{z_R})^2) \tag{3.25}$$

and finally the Guoy phase shift

$$\Phi(z) = tan^{-1}\frac{z}{z_R} \tag{3.26}$$

So we can use this Gaussian beam instead of the fundamental mode profile to model the arrayed waveguide grating. Use of Gaussian beam approximation of fundamental mode profiles of arrayed waveguides can simplify the transfer function of AWG and reduce the computational budget.

3.1.1 Gaussian beam approximation at input FPR

We have modeled the input waveguide mode-profile (see Fig. 3.3) such that the field spread at any point along the propagation direction (z) in input FPR can be accurately estimated and is given by:

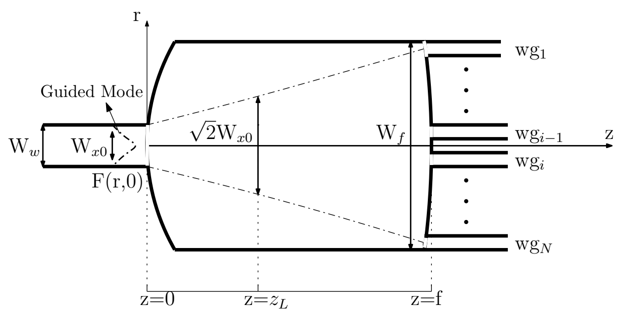

Figure 3.3: Gaussian spreading scheme used for modeling the input FPR W_x is the (1/e) width of the Gaussian approximated guided mode in the r direction, W_w is the width of the waveguide, W_f is the width of FPR region and z_L is the distance at which the (1/e) width becomes $\sqrt{2}W_{x0}$.

$$F(r, z) = A(z)exp[-\frac{\beta_s z_L r^2}{2(z^2 + z_L^2)}] \quad (3.27)$$

where,

$$A(z) = \frac{F_0}{\sqrt{1 + (\alpha z/z_L)^2}} \quad (3.28)$$

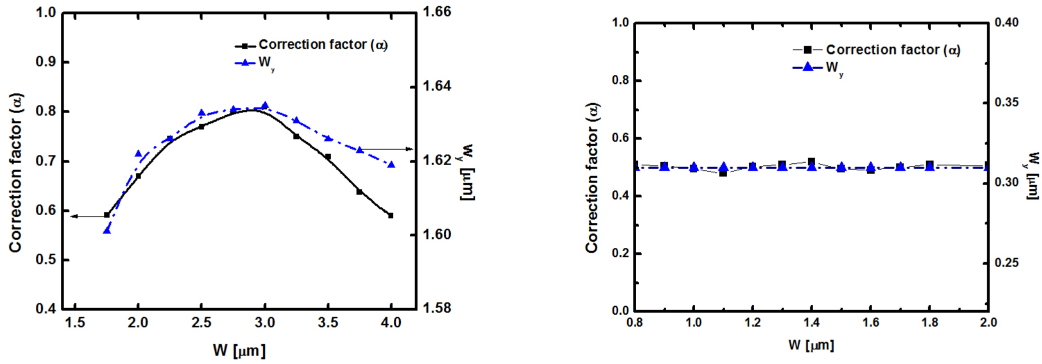

(a) (b)

Figure 3.4: (a) Calculated correction factor (α) and W_y variations (calculated from Lumerical mode Solver) as a function of tapered waveguide width W (interconnecting input waveguide and input FPR) for 2-μm-SOI AWGs; (b) Calculated correction factor (α) and W_y variations as a function of tapered waveguide width W (interconnecting input waveguide and input FPR) for 220-nm-SOI AWGs.

here, z and r are the distance along the propagation direction and transverse direction respectively, F_0 is the peak amplitude at $z = 0$, β_s is the propagation constant of the FPR, z_L is the distance along the propagation direction when width of Gaussian beam becomes $\sqrt{2}$ times the initial width (W_{x0}) and α is the correction factor which accounts for the modal mismatch at the junction between input waveguide and the input FPR. By including α, the effect of W_y variation (calculated from Lumerical Mode Solver) of the mode between waveguide and FPR region for different waveguide widths can be incorporated and α is found to be following the same nature as that of W_y for different waveguide widths (Figs. 3.4(a) and 3.4(b)).

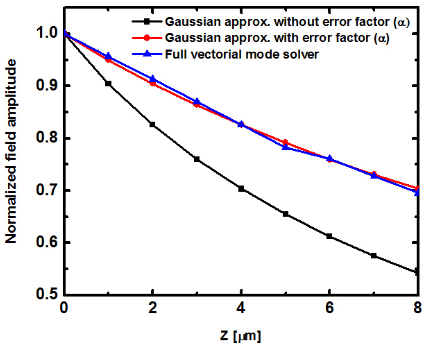

(a)

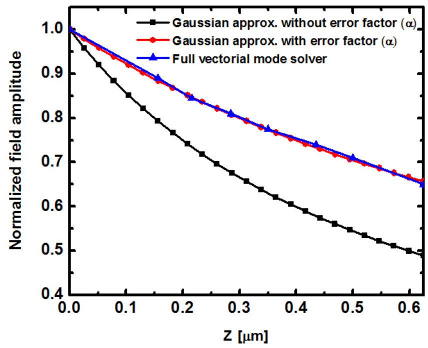

(b)

Figure 3.5: (a) Comparison of electric field amplitude along the propagation direction with and without the correction factor for 2-μm-SOI; (b) Comparison of electric field amplitude along the propagation direction with and without the correction factor for 220-nm-SOI.

Figs. 3.5(a) and 3.5(b) shows the comparison of Gaussian spread with that of full vectorial mode solver in the FPR region with and without α. By including α (as in eqn. 3.27) we can model the Gaussian spread similar to that of numerical calculations. The correction factor (α) is found to be close to 0.8 for a tapered waveguide width of $\sim 2 - 3\ \mu m$ in 2-μm-SOI, since the W_y and the peak position of the waveguide mode were found to be nearly matching with that of the free propagating mode in the FPR region. We have carried out the same analysis of α for photonic wire waveguides (220-nm-SOI) also and irrespective of changing waveguide widths (tapered to 1 μm - 2 μm), W_y and α were found to be nearly constant ($W_y \sim 310\ nm, \alpha \sim 0.5$). Using eqn. (3.27), we calculated the field distribution at the end of input FPR by substituting $z = f$ (focal length of input FPR).

The overlap integral (Γ_i) between this field with each of the arrayed waveguide mode profiles is used to obtain coupled power into the arrayed waveguides. The overlap integral between expanded Gaussian beam with the field with each of the arrayed waveguide mode profiles is calculated using:

$$\Gamma_i = \frac{\left[\int\limits_{-\infty}^{+\infty} F(r)E(r-r_i)dr\right]^2}{\int\limits_{-\infty}^{+\infty} F^2(r)dr \int\limits_{-\infty}^{+\infty} E^2(r-r_i)dr} \tag{3.29}$$

where $E(r - r_i)$ is the mode profile of the arrayed waveguide and r_i is the position of i^{th} arrayed waveguide.

3.1.2 Gaussian beam superposition at output FPR

The output FPR has been modeled again using Gaussian approximation and the wavelength (and phase) dependent interference pattern (Fig. 3.6) can be obtained at the focal plane of output FPR:

$$\Psi(r', \lambda) = \sum_{i=1}^{N} A_i F_i(r') exp[j(\Phi_{1i}) + (\Phi_{2i})] \tag{3.30}$$

where,

$$\Phi_{1i} = \beta_s(2f + (N + 1 - 2i)dr'/2f) \tag{3.31}$$

$$\Phi_{2i} = \beta_i(L_0 + (i - 1)\Delta L) \tag{3.32}$$

here r' is any point on the focal plane of FPR, $\Psi(r', \lambda)$ is the field amplitude at r', N is the number of arrayed waveguides, A_i is the field amplitude of i^{th} arrayed waveguide, $F_i(r')$ is the field amplitude at r' due to the i^{th} arrayed waveguide, β_s and β_i are the propagation constants of FPR and i^{th} arrayed waveguide respectively, L_0 is the length of the smallest arrayed waveguide and $\Delta L$is the incremental length of the arrayed waveguide. The possible non-uniformities of arrayed waveguides were included by suitable variation of propagation constants β_i: $\beta_i = 2\pi(n_{eff} + p_i\Delta n_{eff})/\lambda$, where n_{eff} is the refractive index of designed waveguide, $p_i \in$ [-1,1], and Δn_{eff} is the maximum variation in the effective index from the designed value. Here, the grating circle and Rowland circle curvatures (see Fig. 3.1) are assumed to be straight lines since the

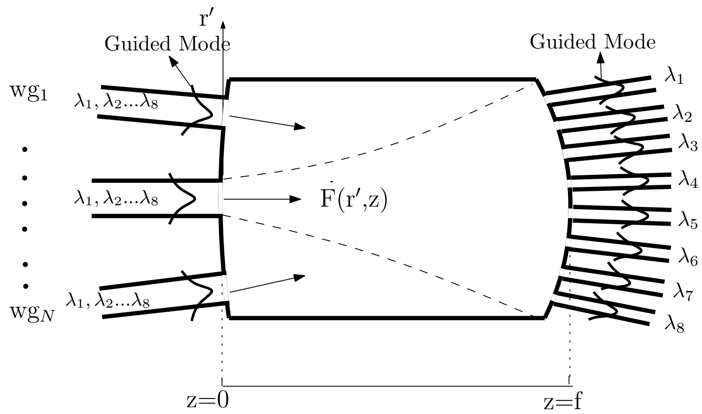

Figure 3.6: Spreading scheme and wavelength dependent interference of Gaussian beams (emerging from the waveguide array) at the focal plane of output FPR.

focal length of FPR is of the order of 100 μm. Now that we have the field profile along the focal plane, an overlap integral (eqn. 3.29) with the output waveguide mode gives us the output power for a particular wavelength.

Fig. 3.7(a) show the comparison of Gaussian approximation method with RSOFT BeamPROP simulation for 8 channel, 100 GHz AWG in 2-μm-SOI with no phase error (assuming correction factor α = 0.59). Fig. 3.7(b) shows the comparison of Gaussian approximation method with experimental results of a 7 channel 200 GHz AWG in 220-nm-SOI [29] (assuming correction factor α = 0.5). In our model, the measured waveguide width variation of $\pm 4nm$ of the fabricated devices has been incorporated by considering a probabilistic distribution among arrayed waveguides as described earlier. We have assumed that the phase-error distribution in each of the waveguides has been taken care by the probabilistic width variation used in the matlab code (see Appendix B). The model however matches well with the experimental results in terms of cross-talk and output spectral distributions.

3.2 Phase Error Analysis

We analyzed the fabrication tolerance of both the AWGs mentioned above using our method. Effective index variation with width (dn_{eff}/dW) was found to be 2.36×10^{-5} (4.38×10^{-5}) nm^{-1} for 2-μm- (220-nm-) SOI waveguides, using which the effect of

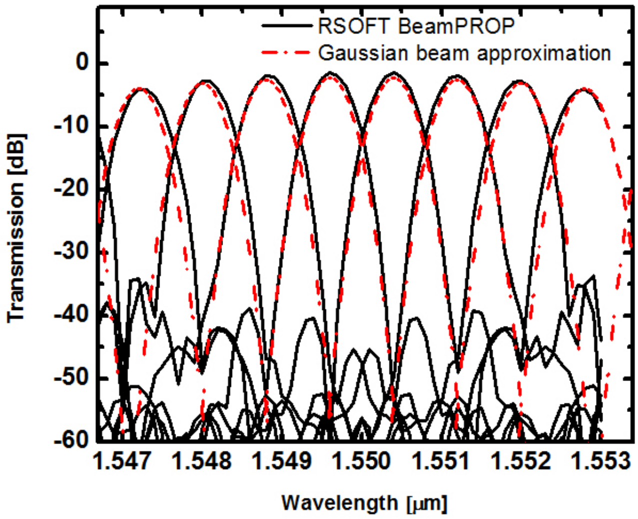

(a)

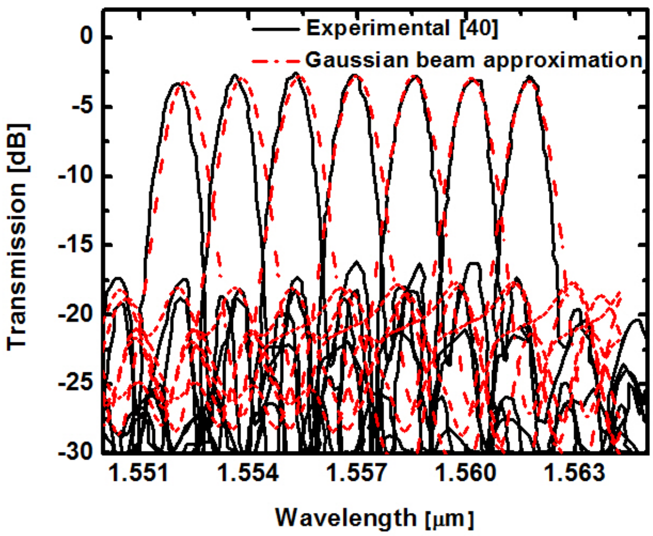

(b)

Figure 3.7: (a) Comparison of output spectrum of 8 channel, 100 GHz AWG in 2-μm-SOI computed by RSoft BeamPROP and Gaussian approximation using α= 0.59; (b) Comparison of experimental results of 7-channel AWG in 220-nm-SOI with Gaussian approximation using α = 0.5.

phase error has been studied. The possible non-uniformities of arrayed waveguides are included by suitable variation of propagation constants β_i: $\beta_i = 2\pi(n_{eff} + p_i\Delta n_{eff})/\lambda$, where n_{eff} is the refractive index of designed waveguide, $p_i \in$ [-1,1], and Δn_{eff} is the maximum variation in the effective index from the designed value which is calculated from dn_{eff}/dW and the maximum width variation obtained (see Fig. 3.8). Here the width has been varied randomly and after analysing the output spectrum using Gaussian beam approximation the crosstalk has been calculated. In order to have a crosstalk level <-10 dB, it is required to control the width variation within $\pm$ 13 nm ($\pm$ 2 nm) for AWG on 2-μm- (220-nm-) SOI. Figs. 3.9(a) and Fig. 3.9(b) illustrate the output spectrum of AWG without and with phase error (corresponding to a width variation of 25 nm). The phase error information can be used for correcting the device characteristics by post-fabrication trimming process [42, 43]

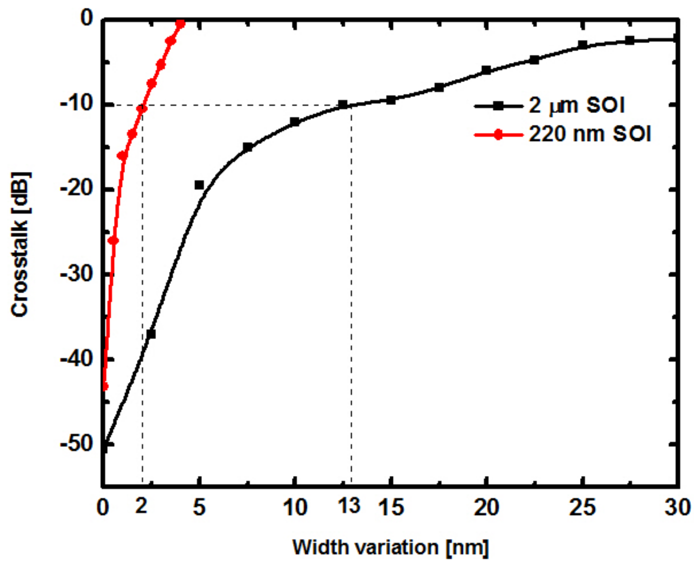

Figure 3.8: Crosstalk degradation as a function of waveguide width variation for AWG on 2-μm-SOI and 220-nm—-SOI (TE polarization).

For the given 2-μm-SOI AWG, BeamPROP simulation takes nearly 35 minutes to complete the simulation (Intel(R) core(TM)i7-2600 CPU @ 3.40 GH processor). AWGs on 220-nm-SOI waveguides which are having high modal confinement, can not be simulated using BeamPROP. For the 220-nm-SOI AWG, 3D FDTD simulation has

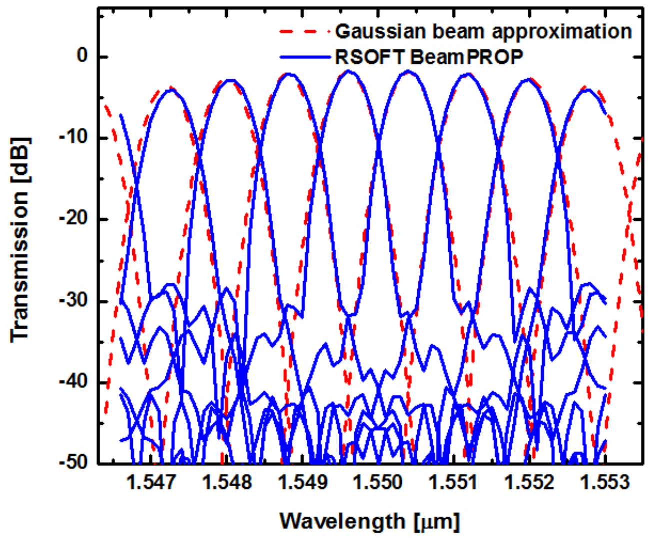

(a)

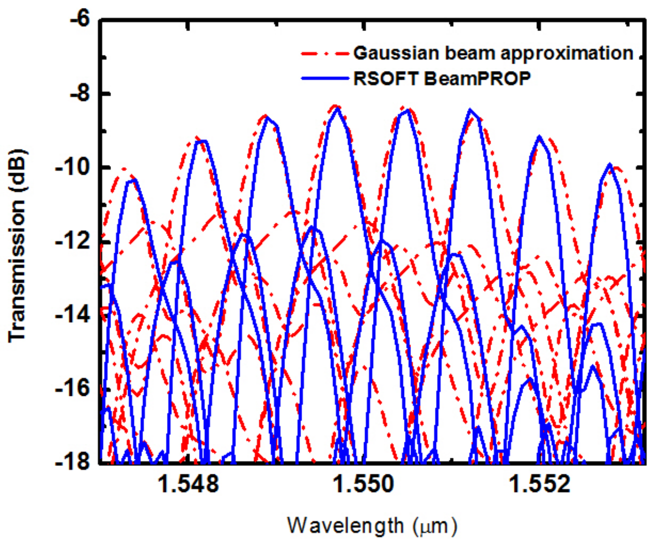

(b)

Figure 3.9: (a) Spectrum of AWG on 2-μm-SOI with no variation in waveguide width; (b) Spectrum of AWG on 2-μm-SOI with probabilistic waveguide width variations of 25 nm.

been carried out, which takes nearly 75 hours to finish with the same processor and demands a huge computational memory. A matlab code for the Gaussian approximation method is found to be consuming less than one minute irrespective of the SOI platform used. However, the coupling information and thereby phase changes due to close proximity regions of arrayed waveguide are neglected in this method.

Similar analysis can be carried out for TM polarization also. Even though the polarization dependency in the FPR region can be neglected, the arrayed waveguides are polarization dependent. So for TM, there will be a lateral shift in the spectrum depending the birefringence($n_{eff}^{TE} - n_{eff}^{TM}$) of the arrayed waveguide geometry. Since the mode profile and W_y of TM mode will be different compared to the TE mode, the correction factor (α) also will be polarization dependent. It is found that α for the 2-μm-SOI AWG, are polarization independent, since the waveguide geometry is having very low birefringence (8.44×10^{-4}). But for 220-nm-SOI AWGs, it is found that α is 0.61 (0.8 $\mu m <$ W $<$ 2 μm) for TM polarization, since the waveguide geometry used are highly polarization birefringent (0.813).

3.3 Summary

A Gaussian beam approximation of guided mode profiles have been developed for analysing the fabrication tolerance of AWG. The method is found to be faster compared to 3D-FDTD and nearly accurate. The method has been evaluated against experimental results and simulated results of R-SOFT BeamPROP and the output spectrum is found to be exactly matching. Using the Gaussian beam approximation method it has been found that in order to have a crosstalk level <-10 dB, it is required to control the width variation within $\pm$ 13 nm ($\pm$ 2 nm) for AWG on 2-μm- (220-nm-) SOI.

CHAPTER 4

Fabrication with i-line Contact Lithography

The phase error analysis using Gaussian beam approximation of guided mode profiles is a faster and accurate method for analyzing the spectrum of AWG. Different lithographic techniques have been adopted for fabrication of AWG. E-beam lithography and deep UV lithography (193-nm) are most commonly used method for fabricating AWGs, since they provide a better structural uniformity and for obtaining ultra small feature size. However, these methods demand huge financial investment. I-line lithography can not be used for very small feature size due to the diffraction limitations but the method is very cost effective. However, feasibility of using i-line lithography in fabrication of AWGs on 2-μm-SOI has not been studied extensively till now. This chapter explains the design and fabrication of optical mask, methodology that can be adopted to fabricate AWG on 2-μm-SOI and waveguide non-uniformity and phase error introduced by i-line lithography fabrication technique. As seen from scheme of AWG structure, some part of the device consist of waveguides which are very close to each other and some other parts which consist of waveguides which are sufficiently far apart. So the fabrication process is challenging and needs to be optimized very carefully. Several experiments had to be done to get an optimized recipe. For optimization, Silicon wafer (p type, $< 100 >$) has been used which is less costly compared to the SOI wafer.

4.1 Photomask Design and Fabrication

The mask layout was created using R-Soft^{TM} [44] CAD tool. The layout consist of two arrayed waveguide structures, five bend waveguides and straight waveguides. In order to account for the fabrication tolerance involved in the mask and device fabrication, AWG structure with different differential length (ΔL) is needed. Hence we have kept two similar set of structures with different ΔL ($\pm$ 5 μm) values. The designed mask is shown in Fig. 4.1. The mask consists of two AWGs which are designed using optimized design parameters. Five numbers of straight and bend waveguide to analyze the loss budget also kept. In addition to this polishing marks were kept in perpendicular to the waveguides which were used for convenience. The sample edges were polished parallel to these markers as it ensures polished edges to be perpendicular to the waveguides.

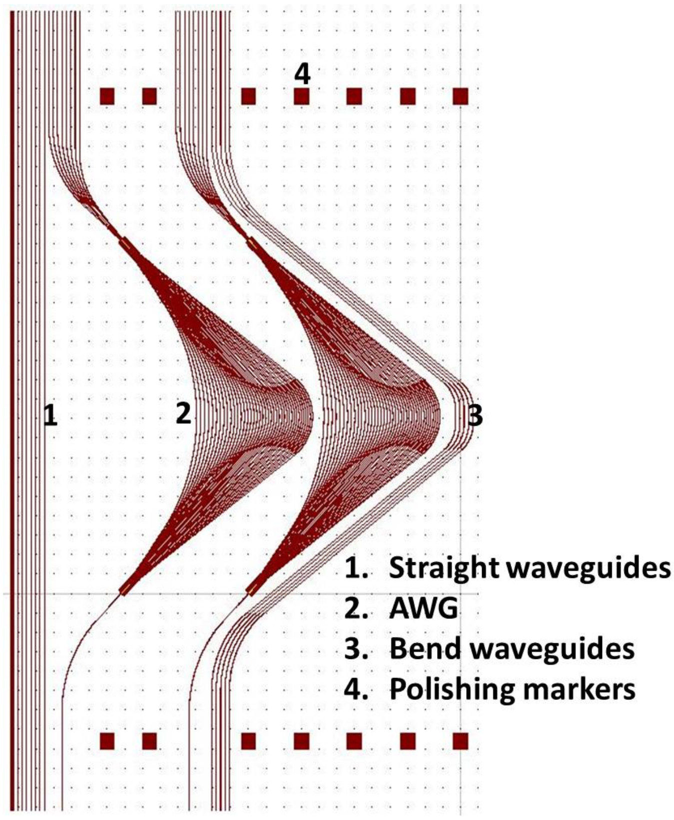

Figure 4.1: Mask layout of designed AWG. The straight and bend waveguides are kept for reference.

This pattern created in R-Soft is converted to Graphic Database System 2 (GDS 2) format. This pattern was subsequently transferred to the photoresist coating on the mask plate using Heilderberg Instruments GmbH^{TM} DWL 66 mask writer (He-Cd laser of λ = 442 nm). Specification of the Japan Laser Corporation mask plate used is given in Table 4.1.

After transferring the pattern on to the photoresist, it was developed using 0.1 M NaOH (5 pellets dissolved in 200 ml DI water) solution. Subsequently, the Chromium etching was done using the Chrome etchant. A mixture of 8 g Ammonium Ceric Nitrate dissolved in 30 ml DI water and 3 ml Glacial Acetic Acid dissolved in 35 ml of DI water were mixed to form the stock solution. Diluting this stock solution in DI water (2:1 ratio) were used as chrome etchant. The remaining PPR was removed by dipping

Table 4.1: Specifications of the mask plate

Parameter	Value
Transparent layer	Fused Silica
Absorbing Layer	Chromium
Photoresist	AZP-1350

the mask plate in Piranha solution ($H_2SO_4 : H_2O_2 :: 3 : 1$) for 5 minutes.

The mask plate after fabrication was carefully analysed in SEM. The critical regions such as 1 μm opening at the input/output FPR - arrayed waveguide junction and the straight waveguides were proper. But the bend region was found to be non-uniform in nature. Finite spot size of mask writer ($\lambda \sim 440\ nm$) leads to wavy nature of bend waveguides, especially since mask writing happens across the pattern rather along the pattern. The SEM images of the mask plates are given in Fig. 4.2

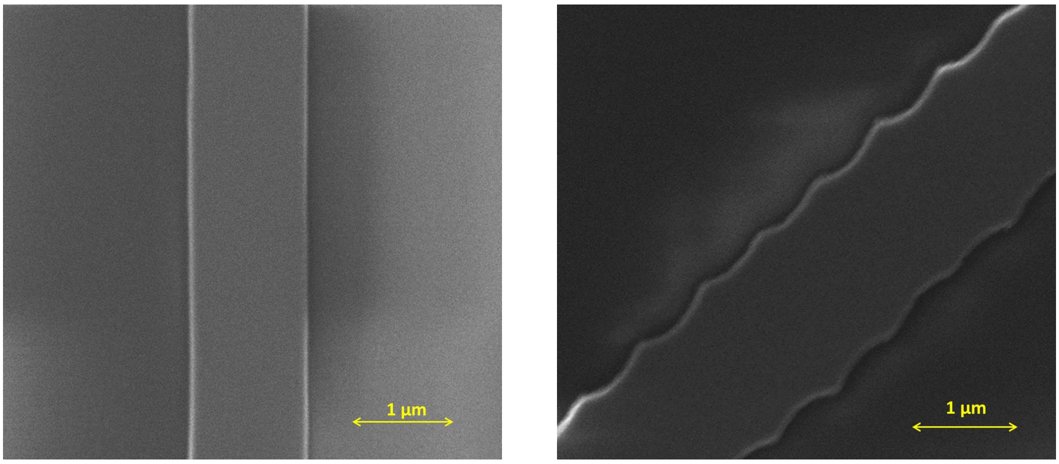

(a) (b)

Figure 4.2: SEM images of mask (a) straight waveguide region for which the waveguide width is found to be uniform; (b) Bend waveguide region for which the width is found to be varying.

4.2 Photolithography and Process Optimization

A standard cleaning procedure has been followed for cleaning the substrate. The substrate was first boiled in TCE (Tri-Chloro Ethylene) for 2-3 minutes to remove all organic impurities. The sample was boiled in acetone to remove the TCE residues and subsequently cleaned in DI water to remove the residues of acetone. Then the sample has been boiled in nitric acid (HNO_3). Since the nitric acid is an oxidising agent, it forms a thin layer of silicon dioxide above the Silicon surface. This is followed by a diluted HF (HF : DI water :: 1 : 10) dip which removes the silicon dioxide on top of the surface and exposes the fresh Silicon layer. The sample has been rinsed thoroughly. Before spin coating, sample was baked for 5 minutes at 120^{0}C to remove the moisture and allowed to cool down. The cleaning procedure was followed by the spin coating of positive Microposit^{TM} photoresist S1813 G2. The spin coating parameters are given in Table 4.2.

Table 4.2: Spin coating parameters of S1813 G2

Parameter	Value
Speed	5000 rpm
Accelaration	600 rpm/sec
Time	45 sec

The thickness of spin coated photoresist has been measured using confocal microscope and the thickness was found to be around 800 nm and found to be uniform in nature except at the edges which does not affect the fabrication of the device. The prebaking was done at 80^{0}C for 28 minutes and thickness got reduced to 700 nm. This was to harden the PPR and to avoid sticking of the PPR when it comes in contact with the optical mask. MA6/BA6 mask aligner is used to align the sample with the AWG optical mask and exposed it with i-line UV (Wavelength : 365 nm, Intensity : 13 mW/cm^2). A post exposure bake has been carried out on the exposed sample at 120 ^{0}C for 5 minutes to reduce the concentration gradient created during the exposure and to slow down the overall developing rate to overcome the difficulty of developing a sample where we have a dense array of waveguides.

Table 4.3: Optimized etching recipe

Parameter	Value
Gas flow rate	SF_6 : Ar :: 20 sccm : 20 sccm
Temperature	20^0C
Pressure	200 mTorr
DC bias	33 V
RF power	150 W
Etch rate	0.33 μm/min

The samples were developed using 0.1 M NaOH solution. Before RIE, the sample has been postbaked at 120 ^{0}C for 30 minutes to harden the PPR. The time of prebake/-postbake, spin coating parameters and developing/exposing time have been optimized after several trial and error. The obtained PPR pattern has been subsequently transferred to the silicon sample by Reactive Ion Etching (RIE). SF_6 : Ar recipe is an optimized recipe which gives very low sidewall roughness ($\sim$ 10 nm). Various devices including spot size converters [45], interleavers [46], high efficient DBR structures [47] etc., have been fabricated and successfully demonstrated using this recipe in our lab. The RIE recipe used has been shown in Table 4.3. The entire procedure followed for the fabrication of AWG device is explained in Fig. 4.3.

The confocal microscopic image of the fabricated sample is shown in Fig. 4.4. The 1 μm separation between arrayed waveguides near FPR region were underdeveloped. At the same time the arrayed waveguides in the middele region of AWG which are sufficiently far apart were washed off. It is confirmed that developer solution takes more time to develop the exposed PPR in the 1 μm region.

So, it is understood that the developing had to be slowed down, so that the 1 μm separation between arrayed waveguides near input/output FPR gets developed properly. Also it is important to make sure that the middle region where arrayed waveguides are well apart does not get overdeveloped. In order to achieve this, we increased the post exposure baking time to 10 minutes. This will slow down the entire developing process.

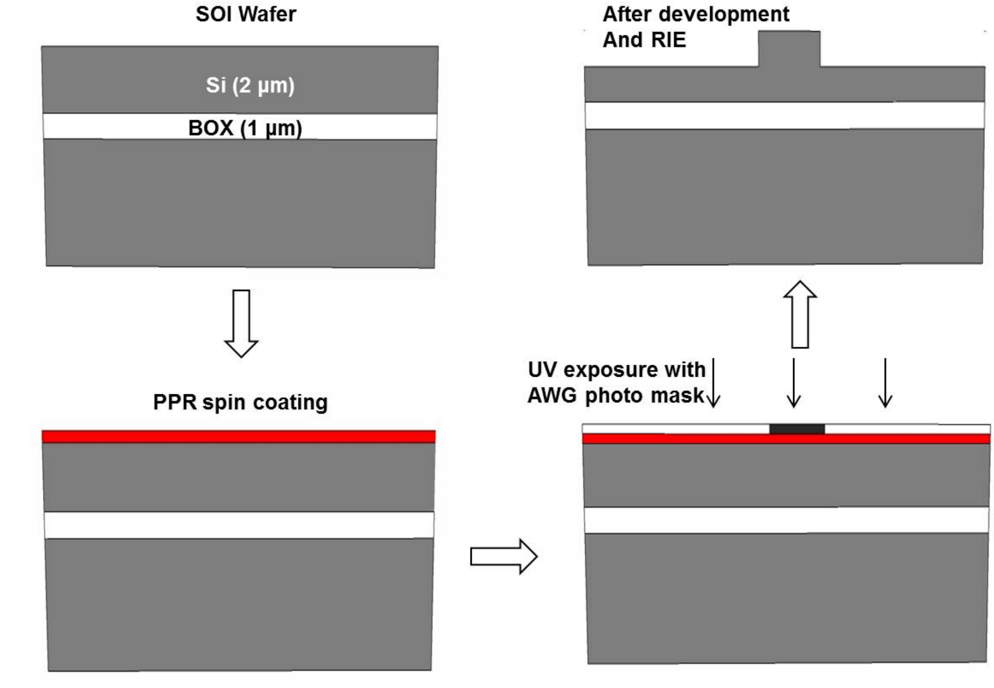

Figure 4.3: Fabrication process flow.

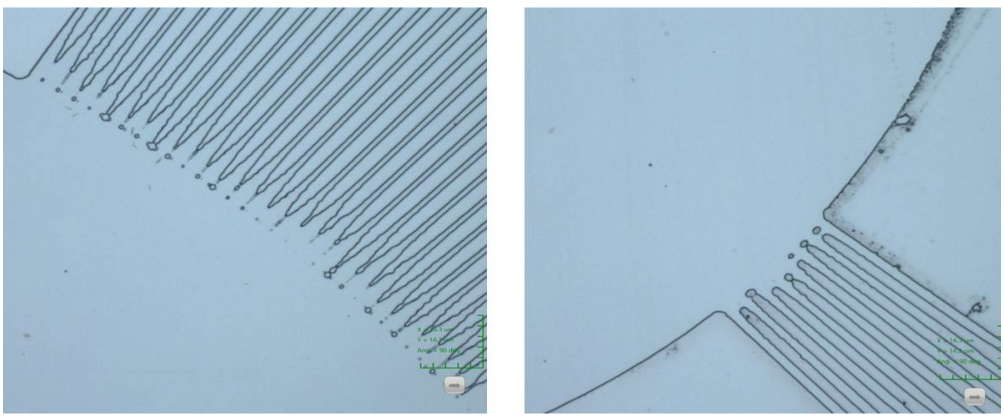

Figure 4.4: Confocal microscopic image of arrayed waveguides near input FPR and output waveguides near output FPR.

It was observed that the opening of 1 μm was not proper and arrayed waveguides in the middle region were getting overdeveloped. But the waveguides were of wavy nature and the developing time was very high. The confocal microscopic image (resolution : 120 nm) of the resulting sample is shown in Fig. 4.5.

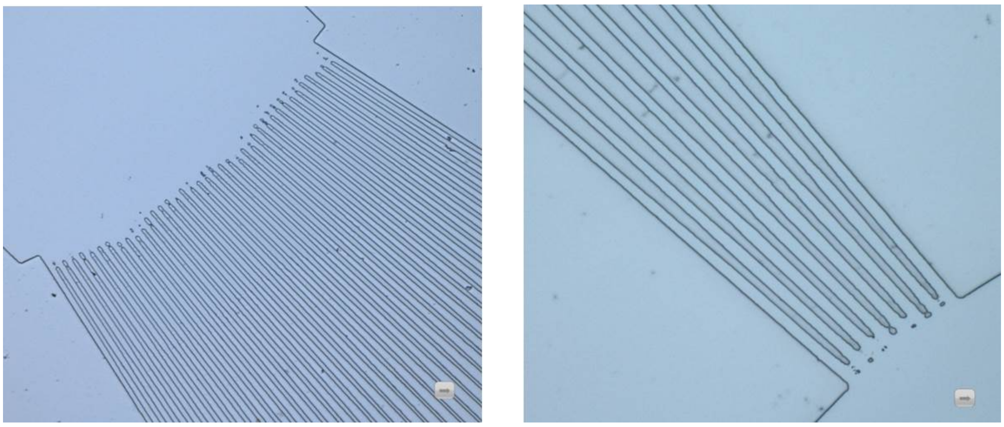

Figure 4.5: Confocal microscopic image of arrayed waveguides near input FPR and output waveguides near output FPR.

The concentration gradient of the developing solution will have a huge impact on the photolithography procedure. So, instead of using prepared NaOH solution, a standard developer should provide better results. We followed the same procedure explained above, by using standard developer MF 321 instead of NaOH solution. The wavy nature of the waveguides which were observed earlier were still present, but the 1 μm openings were better compared to earlier structure. The confocal microscopic image of the developed samples are given in Fig. 4.6.

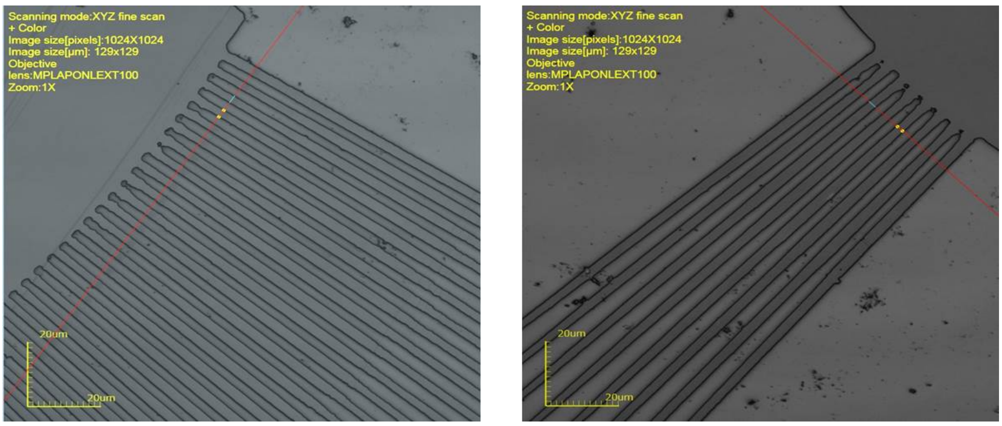

Figure 4.6: Confocal microscopic image of arrayed waveguides near input FPR and output waveguides near output FPR.

We were able to conclude that the conventional lithographic procedures can not be directly adopted to get a satisfactory structure of AWG. Descum [48] is a method used to remove the photoresist residues from the sample after fabrication. This approach will be of great help in optimizing the recipe to get the required dimension. The sample was developed till the waveguides in the middle region was proper. It is obvious that the 1 μm separation will be underdeveloped. At this point if the thickness of the PPR is reduced by Descum process (reduced by $\sim$ 150 nm), it would lead to the proper opening of 1 μm separation without overdeveloping the arrayed waveguides in the middle region. The descum recipe used, is shown in Table 4.4.

Table 4.4: Optimized descum recipe

Parameter	Value
Gas flow rate	O_2 : 50 sccm
Temperature	20^0C
Pressure	100 mTorr
ICP Power	150 W
RF power	150 W
Etch rate	0.18 μm/min
Time	50 seconds

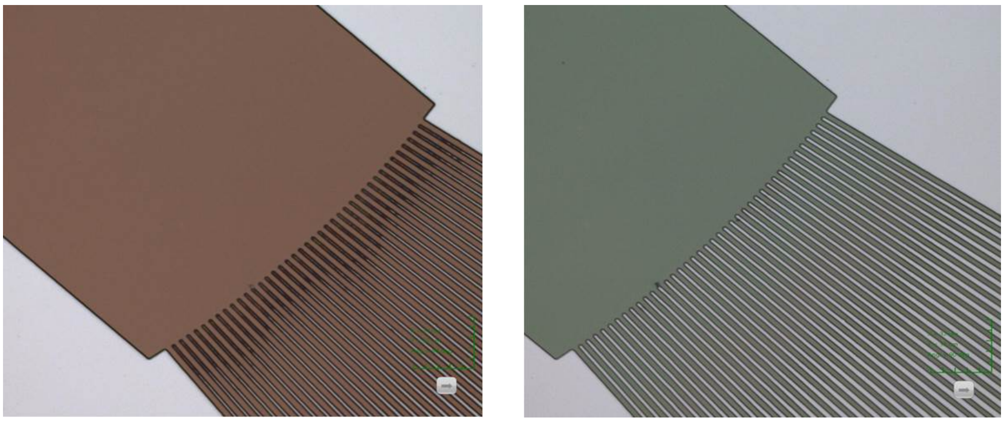

Figure 4.7: Confocal microscopic image of arrayed waveguides near input FPR before and after the descum.

The confocal microscopic image of the perfect 1 μm opening near input FPR before and after the descum is shown in Fig. 4.7. This optimized recipe has been used for fabricating the designed AWG on a SOI (Device layer thickness : 2 μm, Resistivity : 5000 $\Omega/\ cm$, Crystal orientation : <100>, Make : Ultrasil inc. USA) sample. The fabricated AWG found to have a uniform separation of 1 μm separation (verified using SEM imaging) and properly developed arrayed and input/output waveguides. The confocal microscopic images of the PPR pattern of AWG fabricated on SOI is given in Fig. 4.8 and the sample after RIE is shown in Fig. 4.9.

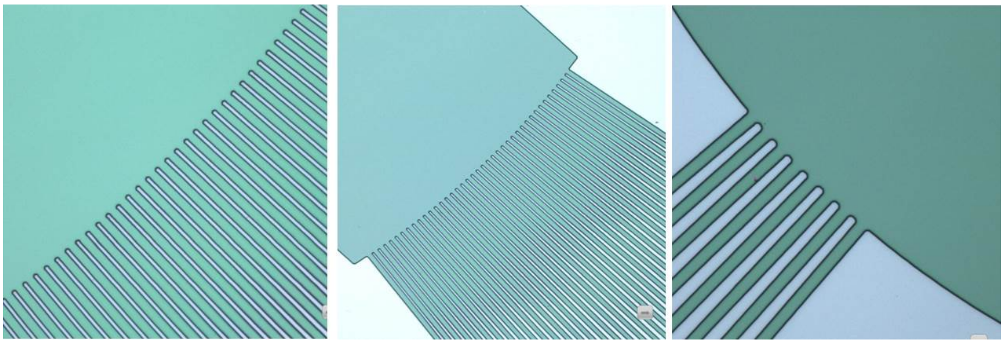

Figure 4.8: Confocal microscopic images of PPR patterns of fabricated AWG on SOI.

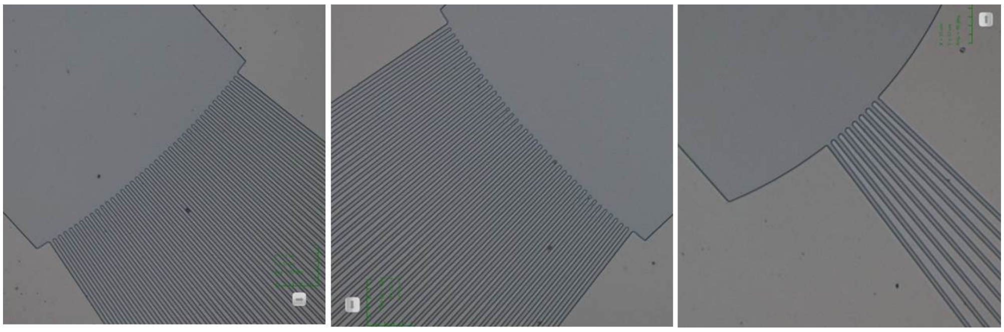

Figure 4.9: Confocal microscopic images of fabricated AWG on SOI after RIE.

The width of the arrayed waveguides are very crucial in AWG design on SOI platform. In order to analyze the phase error introduced by the arrayed waveguides, width of arrayed waveguides were measured using SEM imaging technique. There was an average width variation of $\pm$ 100 nm. The SEM images of three different arrayed waveguides of the same AWG is shown Fig. 4.10. We observed a lengthwise non-uniformity of around $\pm$ 40 nm for all the arrayed waveguides (as shown in Fig. 3.27).

Focusing high energy electron beam on SOI creates charging problem, because of the oxide layer beneath the device layer. So we have coated a thin layer of gold (10 nm) to discharge the accumulated charges. The white particles in the SEM images are nothing but the gold particles coated on the SOI sample.

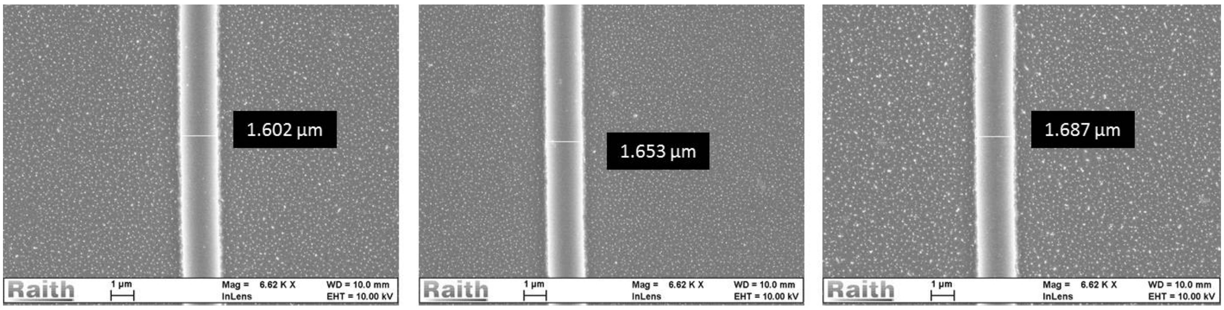

Figure 4.10: SEM images of three arrayed waveguides showing the width variation in arrayed waveguides.

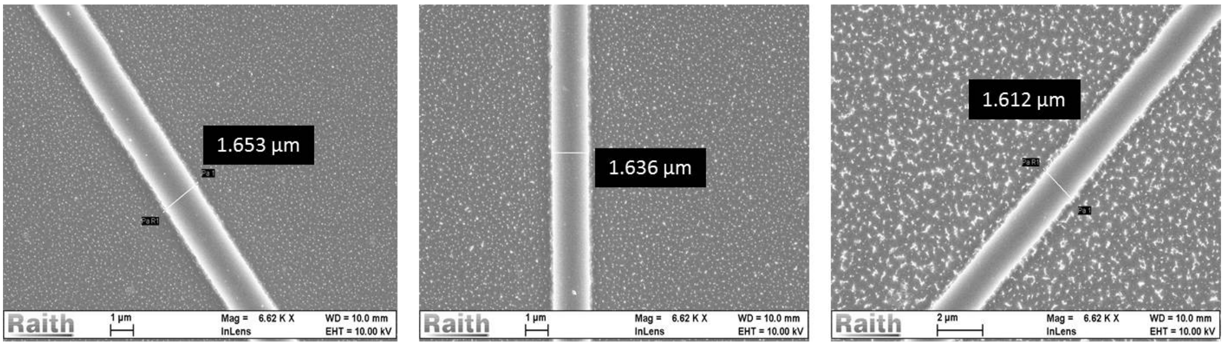

Figure 4.11: SEM images of a sample arrayed waveguide showing the lengthwise width variation.

Similarly we have analyzed the waveguide widths of all the forty arrayed waveguides and plotted in Fig. 4.12. The red line in the Fig. 4.12 shows the waveguide widths of the designed AWG and the black line shows the waveguide widths of the fabricated device. The waveguide width has been found to be varying between 1.6 μm and 1.7 μm. Hence, we observed a maximum width variation of $\pm$ 100 nm in the arrayed waveguides.

For the center wavelength to have constructive interference at the middle of the output focal plane, the phase front of the waves through all the arrayed waveguides should be an integral multiple of 360^0. Because of the distortion in the waveguide width, the phase front of the wave will also be distorted. The possible non-uniformities of arrayed waveguides are included by suitable variation of propagation constants β_i: $\beta_i = 2\pi(n_{eff} + p_i \Delta n_{eff})/\lambda$, where n_{eff} is the refractive index of designed waveguide, $p_i \in$ [-1,1], and Δn_{eff} is the maximum variation in the effective index from the designed

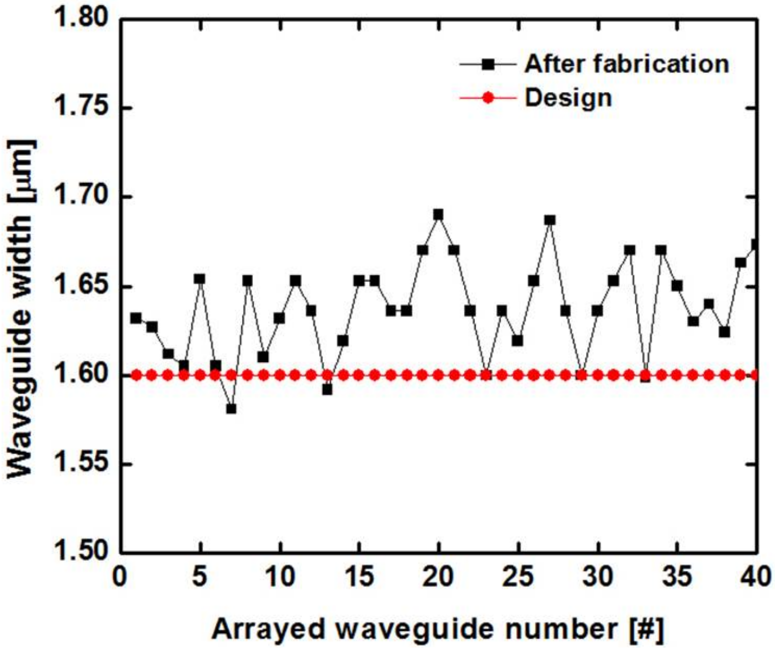

Figure 4.12: Waveguide width plotted against the arrayed waveguide number.

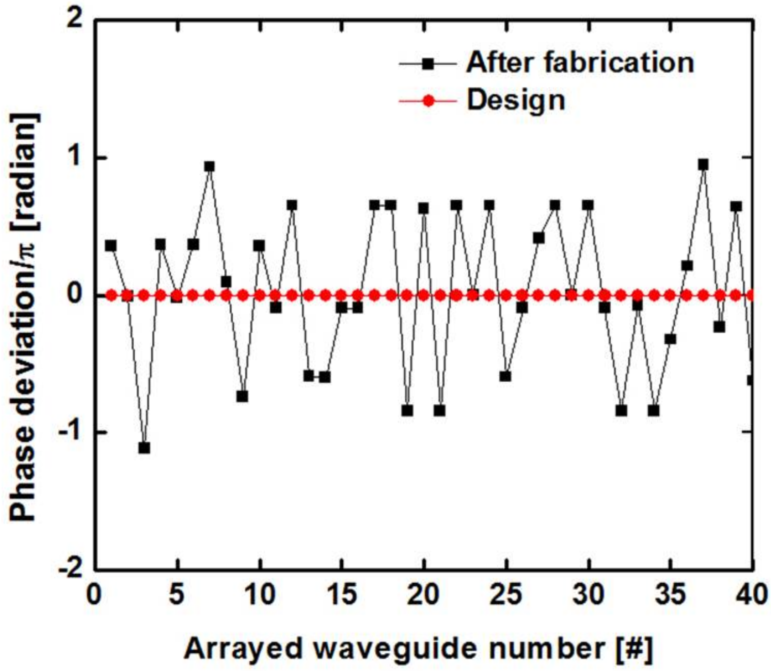

Figure 4.13: Waveguide width plotted against the arrayed waveguide number.

value which is calculated from dn_{eff}/dW and the maximum width variation obtained (see Fig. 3.8). For the center wavelength, the phase front expected if all the arrayed waveguides are of same waveguide width, is shown in red color and the phase front of fabricated device with width variation is shown using black line in Fig. 4.13

4.3 Summary

From the Fig. 4.13 and Fig. 3.8 it can be concluded that, the phase front distortion produced by this width variation in the arrayed waveguides is too high to produce any interference pattern at the output. Even though the fabrication processes are carefully optimized to get a near perfect structure, it is found to be very difficult to keep the arrayed waveguide width constant throughout the footprint of the device. Even a 25 nm width variation is found to create a huge distortion in the phase front of the device. Hence the width variation of $\pm$ 100 nm introduced due to i-line lithography and subsequently by the etching process is too high to get a satisfactory performance. It is concluded that i-line lithography is not the optimum technique for fabricating such a fabrication sensitive device like AWG and feasibility of improving the fabrication techniques using i-line lithography, deep UV lithography (Wavelength: 193 nm) and e-beam lithography for AWG can be explored further.

CHAPTER 5

Conclusions

5.1 Summary

In this work, study of the fabrication tolerance of AWGs has been done. We proposed a semi-analytical method to analyze the AWG using Gaussian beam approximation of guided mode profiles which will be faster compared to the commercial FDTD design tools and nearly accurate. This method has been used to analyze fabrication tolerance of AWGs on different device layer thickness. Fabrication tolerance of i-line lithography also has been studied after fabricating AWG with i-line lithography.

Chapter 2 explains the design of AWGs on 2-μm-SOI and 220-nm-SOI. Design parameters are carefully chosen to minimize the losses and to make the structure as compact as possible. Restriction in defining structures using i-line lithography techniques has also been considered while designing the device. The effect of various parameters such as waveguide dimensions, separation between arrayed waveguides and output waveguides, number of arrayed waveguides and bend radius, on AWG characteristics has been studied. Numerical methods are not ideal for simulating AWG and analysing fabrication induced phase errors. They demand huge computational budget due to the large footprint and small features of the device. Chapter 3 explains modeling of AWGs on SOI using Gaussian beam approximation of guided mode profiles. A semi-analytical model has been developed in which Gaussian beam approximation is used for guided mode profiles to analyze the output spectrum of AWGs. The AWG output spectrum simulated using our method has been compared with the existing numerical methods and found to be reasonably accurate even for high refractive index contrast photonic wire waveguide based compact AWGs in SOI platform. It has been also shown that this model can be used to extract phase errors (due to waveguide non-uniformities) from experimental results. In order to get a crosstalk $<$ -10 dB, the tolerable width variation in the arrayed waveguides has been found to be $\pm$ 13 nm ($\pm$ 2 nm) for AWG fabricated on 2-μm-SOI (220-nm-SOI).

Chapter 4 explains the fabrication of AWG on 2-μm-SOI using i-line lithography. AWG designed on 2-μm-SOI has been successfully fabricated by introducing Descum process step with the i-line lithographic technique. The error estimation of the fabricated structure has been done using the Gaussian approximation model developed in chapter 3. It has been found that a width variation of around $\pm$ 100 nm has been observed which is above the tolerable limit. A necessary post-fabrication trimming of waveguides can be employed to rectify the phase errors.

5.2 Future Scope of work

AWGs were found to be a highly fabrication sensitive device. The phase errors introduced due to fabrication imperfection is a major concern. Some suggestions for improving the device performance are listed below.

1) More sophisticated and improved lithographic techniques can be used to fabricate AWG on 2-μm-SOI. E-beam lithography can be optimized to fabricate AWG on 220-nm-SOI, which can be used to fabricate very fine features and the phase error introduced by e-beam lithography has proven to be minimal.

2) The phase error analysis using Gaussian beam approximation has been done assuming random widths for arrayed waveguides. The lengthwise width variation has been neglected in all the simulations. The phase error introduced by AWG can be analyzed using Gaussian beam approximation method by obtaining the exact width variation of fabricated AWG, based on which the Gaussian approximation method can be further improved. Once an AWG is fabricated within the tolerable width variation, the AWG can be experimentally tested. The experimental results can be compared with Gaussian beam approximation method after including all the structural features of the fabricated device.

Appendix A

Rowland circle theorem - Proof

Consider the figure shown below. The arc PQ is part of a grating circle with center at C and radius R. Let us assume that we have a source at D. Let any two rays coming from D is reflecting from A and B_1 and makes an image at E. The path length difference between these two rays should be an integer multiple of wavelength (λ) to have a constructive interference at E. Let us assume that the distance between two reflecting points be d and its value is much less than the radius R.

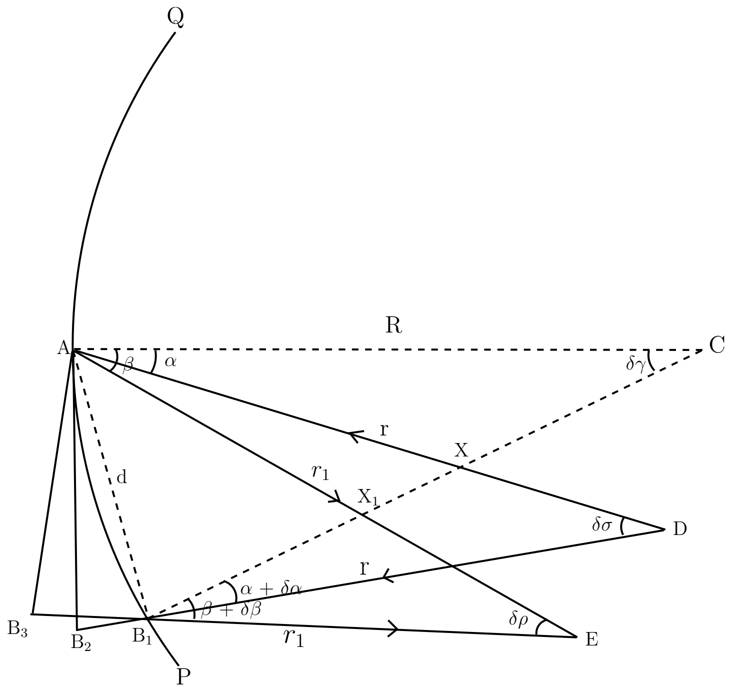

Figure 5.1: Rowland circle geometry proof, D is the source and E is the point where image is assumed to be formed.

divisors From figure, we can write the condition for interference at E using grating equation,

$$dsin(\alpha) + dsin(\beta) = m\lambda \tag{5.1}$$

Differentiating eqn. 5.1 with respect to α, we get

$$cos(\alpha)\delta\alpha + cos(\beta)\delta\beta = 0 \tag{5.2}$$

Consider $\triangle AXC$ and $\triangle B_1XD$,

$$\angle AXC = \angle B_1XD \tag{5.3}$$

From $\triangle AXC$,

$$\angle AXC = 180^o - \angle XCA - \angle CAX \tag{5.4}$$

$$\angle AXC = 180^o - \delta\gamma - \alpha \tag{5.5}$$

Similarly from $\triangle B_1XD$,

$$\angle B_1XD = 180^o - \angle XDB_1 - \angle DB_1X \tag{5.6}$$

$$\angle B_1XD = 180^o - \delta\sigma - (\alpha + \delta\alpha) \tag{5.7}$$

From eqns. 5.3, 5.5 and 5.7, we can conclude

$$\delta\alpha = \delta\gamma - \delta\sigma \tag{5.8}$$

Similarly from $\triangle AX_1C$ and $\triangle B_1X_1E$, we can write

$$\delta\beta = \delta\gamma - \delta\rho \tag{5.9}$$

Now from Fig. 5.1, we can write

$$\delta\gamma = \frac{AB_1}{R} \tag{5.10}$$
$$\delta\sigma = \frac{AB_2}{r} = \frac{AB_1cos(\alpha)}{r} \tag{5.11}$$
$$\delta\rho = \frac{AB_3}{r_1} = \frac{AB_1cos(\beta)}{r_1} \tag{5.12}$$

Substituting eqns. 5.10, 5.11 and 5.12 in eqn. 5.8 and 5.9, we get

$$\delta\alpha = \frac{AB_1}{R} - \frac{AB_1cos(\alpha)}{r} \tag{5.13}$$
$$\delta\beta = \frac{AB_1}{R} - \frac{AB_1cos(\beta)}{r_1} \tag{5.14}$$

Substituting eqns. 5.13 and 5.14 in eqn. 5.2, we get

$$cos(\alpha)[\frac{AB_1}{R} - \frac{AB_1cos(\alpha)}{r}] + cos(\beta)[\frac{AB_1}{R} - \frac{AB_1cos(\beta)}{r_1}] = 0 \tag{5.15}$$

The only solution to the eqn. 5.15 is

and

$$r = Rcos(\alpha) \tag{5.16}$$
$$r_1 = Rcos(\beta) \tag{5.17}$$

Eqns. 5.16 and 5.17 confirms that C, D and E are lying on the circumference of the circle with diameter R called the Rowland circle. Hence the proof.

Appendix B

Matlab code used for simulating AWG transfer function using Gaussian beam approximation

```
tic;
clc;
clear all;
close all;
W=1.6e-6;         %% Rib width of waveguide
RH=2e-6;          %% Rib height of waveguide
sh=1e-6;          %% slab height of waveguide
n1=3.4777;         %% refractive index of Silicon
n2=1.45;           %% Refractive index of BOX
n3=1;              %% refractive index of air
lambda=1549.5e-9;         %% centre wavelength
dlam=0.5e-9;
ewit=1.8e-6;        %% (1/e) Width of input taper mode
wit=2e-6;           %% Width of input taper
ewa=1.8e-6;         %% (1/e) Width of array taper mode
wa=2e-6;            %% Width of array taper
ewot=1.8e-6;        %% (1/e) Width of output taper mode
wot=2e-6;             %% Width of output taper
da=1e-6;            %% Separation between arrayed waveguide
dit=1e-6;           %% Separation between input waveguide
dot=1e-6;           %% Separation between output waveguide
warray=wa+da;        %% Center-center separation of arrayed waveguide
winput=wit+dit;      %% Center-center separation of input waveguide
woutput=wot+dot;      %% Center-center separation of output waveguide
neffcl=zeros(1,3);
nfcl=zeros(1,3);
neffc=zeros(1,3);
nfc=zeros(1,3);
neff=zeros(1,3);
```

```
     %%%%    Finding effective index of core region %%%%%%%
for p=1:3;

 ttacl=asin(n2/n1);
 ttacu=asin(n3/n1);
 a=ttacu;
 ttai=a:0.0001:pi/2;
 phil=2.*(atan(sqrt(((n1/n2)^2).*((sin(ttai)).^2)-1)./((n1/n2).*cos(ttai))));
 phiu=2.*(atan(sqrt(((n1/n3)^2).*((sin(ttai)).^2)-1)./((n1/n3).*cos(ttai))));
 phi=phil+phiu;
 phi1=phil+phiu+(2*pi);
 k=(2*pi)/(lambda);
 h=RH;
 b=2.*n1.*h.*k.*cos(ttai);
 i=1;
 while(phi(i)<b(i))
  theta=ttai(i);
  i=i+1;
 end
 neffc(p)=n1*sin(theta);
 nfc(p)=neffc(p);
 h=sh;
 b=2.*n1.*h.*k.*cos(ttai);
 i=1;
 while(phi(i)<b(i))
  theta=ttai(i);
  i=i+1;
 end
 neffcl(p)=n1*sin(theta);
 nfcl(p)=nefcl(p);

            %%%%%%% Effective index of cladding %%%%%%%%

 ttacl=asin(neffcl(p)/neffc(p));
 ttacu=asin(neffcl(p)/neffc(p));
 a=ttacu;
 ttai=a:0.0001:pi/2;
```

```
 Ai=((nfcl(p)/nfc(p)).*cos(ttai));
 phil=2.*(atan(sqrt(((nfc(p)/nfcl(p))^2).*((sin(ttai)).^2)-1)./Ai));
 phiu=2.*(atan(sqrt(((nfc(p)/nfcl(p))^2).*((sin(ttai)).^2)-1)./Ai));
 phi=phil+phiu;
 k=(2*pi)/(lambda);
 h=W;
 b=2.*neffc(p).*h.*k.*cos(ttai);
 i=1;
 while(phi(i)<b(i))
  theta=ttai(i);
  i=i+1;
 end
 neff(p)=neffc(p)*sin(theta);
 lambda=lambda+dlam;
end
              %%%%%    Finding effective index of array taper  %%%%%%%%%%%
 lambda=1.55e-6;
 ng=neff(2)-((lambda*(neff(3)-neff(1)))/(2*dlam));
 a=ttacu;
 ttai=a:0.0001:pi/2;
 Ai=((nfcl(2)/nfc(2)).*cos(ttai));
 phil=2.*(atan(sqrt(((nfc(2)/nfcl(2))^2).*((sin(ttai)).^2)-1)./Ai));
 phiu=2.*(atan(sqrt(((nfc(2)/nfcl(2))^2).*((sin(ttai)).^2)-1)./Ai));
 phi=phil+phiu;
 phi1=phil+phiu+(2*pi);
 k=(2*pi)/(lambda);
 h=wa;
 b=2.*neffc(2).*h.*k.*cos(ttai);
 i=1;
 while(phi(i)<b(i))
  theta=ttai(i);
  i=i+1;
 end
 neff0=neffc(2)*sin(theta);
 nwa=neff0;

     %%%%%    Finding effective index of input/output taper  %%%%%%%%%%%
```

```
 h=wit;
 b=2.*neffc(2).*h.*k.*cos(ttai);
 i=1;
 while(phi(i)<b(i))
  theta=ttai(i);
  i=i+1;
 end
 neff0=neffc(2)*sin(theta);
 nwit=neff0;
 nwot=nwit;



  %%%  THIS IS A PROGRAM TO ANALYZE AWG TRANSFER FUNCTIONS ANALYTICALLY
%%%%%%%%%%

              %%%%% CODING DONE BY SIDHARTH - IOLAB %%%%%%%%%%%%

                  %%% Effective index definition%%%


nsi=3.4777;          %% Silicon refractive index
ns=neffc(2);         %% Effective index of 2 micron slab
neffTM=neff(2);      %% TM polarisation effective index.
d_w=22200;           %% dneff/dw for rcrw
dw=0;                %% maximum width variation
dneff=dw*d_w;        %% maximum effective index variation

             %%% Parameters of AWG %%%%

lambdac=1.55e-6;
dlambda=0.8e-9;
nchan=8;
FSR=nchan*dlambda;
Na=40;
Lo=2e-4;
lambdastart=(lambdac-((FSR+dlambda)/2));
lambdastop=(lambdac+((FSR+dlambda)/2));
```

```matlab
%%%% Loop variables %%%%%%%%

count=20000;
count_plot=400;
count_lambda=65;
extra=(Na*warray)/count;
extrainput=wit/(count_plot);
extraoutput=2*wot/(count_plot);
tunelambda=(lambdastop-lambdastart)/(count_lambda-1);

%%% Defining arrays %%%%%

p=rand(1,Na);
neff1=zeros(1,Na);
Beff=zeros(1,Na);
Ef=zeros(1,count);
FVABS=zeros(count_plot+1,count_lambda);
FVABS2=zeros(count_plot+1,count_lambda);
OUTCOUPLE=zeros(count_plot,count_lambda);
CC=zeros(1,count_lambda);
C=zeros(1,count_lambda);
H=zeros(count_lambda,nchan);
y=zeros(1,count_lambda);
A=zeros(1,Na);
G=zeros(1,Na);
G1=zeros(1,Na);
L=zeros(1,Na);
O=zeros(1,Na);
B1=zeros(1,count);
Ey=zeros(1,count+1);
Ey1=zeros(1,count_plot+1);
Eyy=zeros(1,count+1);
Eyy1=zeros(1,count_plot+1);

%%% Calculated Parameters %%%
```

```
w=2*pi/lambdac;
kit=w*nwit;
ka=w*nwa;
kot=w*nwot;
xlower=-((Na*(wa))+(Na-1)*da)/2;
xupper=-(((Na-2)*(wa))+((Na-1)*da))/2;
zra=(pi*nwa*(wa/2)*(wa/2))/lambdac;
zrit=(pi*nwit*(wit/2)*(wit/2))/lambdac;
zrot=(pi*nwot*(wot/2)*(wot/2))/lambdac;
gratingorder=round((neff(2)*lambdac)/(nchan*dlambda*ng));
f=(ns/gratingorder)*((warray*winput)/dlambda);
dL=gratingorder*lambdac/neff(2);
xincr=(wa)/(count);

a0=(xupper+xlower)/2;

corrAmpArray=0.55;
corrAmpInput=0.55;
corrphasearray=1;
corrphasein=1;


          %%%%%%%%%%%%%%% INPUT FPR BEGINS %%%%%%%%%%%%%%

x=-(wa)/2;
for l=1:(count+1);
    Ey(l)=exp(-(ka*x*x)/(2*zra));
    Eyy(l)=Ey(l)*Ey(l);
    x=x+xincr;
end


x=linspace((-wa)/2,(wa)/2,count+1);
Amp=trapz(x,Eyy);
Z=1/(1+(0.414*corrAmpInput*(f/zrit)));
x=linspace(-(Na*warray)/2,(Na*warray)/2,count+1);
B2=(Z)*exp(-(kit*zrit.*x.*x)/(2*((f^2)+(zrit^2))));
Amp1=trapz(x,B2.*B2);
```

```
for j=1:Na
        x=-(Na*warray)/2;
        a1=(j-1)*warray+a0;

            for l=1:count+1;

              if((xlower+((j-1)*warray))<x && x<(xupper)+((j-1)*warray));
               Ef(l)=(1/sqrt(Amp))*exp(-(ka.*(x-a1).*(x-a1))/(2*zra));
              else
               Ef(l)=0;
            end
        x=x+extra;

end
x=linspace(-(Na*warray)/2,(Na*warray)/2,count+1);
       G(j)=trapz(x,(B2.*Ef));
       G1(j)=G(j)*G(j);
       J=trapz(x,(Ef.*Ef));
       K=(J*Amp1);
       L(j)=G1(j)/(K);
       A(j)=sqrt(L(j)/Amp);
end


             %%%%%% INPUT FPR ENDS HERE %%%%%%%%%



            %%%%%%% OUTPUT FPR BEGINS %%%%%%%%%%%%



do=-(nchan-1)*woutput/2;
lambdac=1.55e-6;
x=-(wot);
w=2*pi/lambdac;
```

```
for l=1:(count_plot+1);
    Ey1(l)=exp(-(kit*x*x)/(2*zrit));
    Eyy1(l)=Ey1(l)*Ey1(l);
    x=x+extraoutput;
end

x=linspace(-(wot),(wot),count_plot+1);
Amp=trapz(x,Eyy1);

for k=1:nchan;
  filename='inputFPRfields.xlsx';
  O=xlsread(filename);
  A=sqrt(O2/Amp);
  phi=zeros(Na,Na);
  phiexp=zeros(Na,Na);
  lambda=lambdastart;

  for j=1:count_lambda;
   Z=1/(1+(0.414*corrAmpArray*(f/zra)));
   w=2*pi/lambda;
   BS=w*ns;
   phis=BS*2*f;
   x=do-(wot);
   for n=1:count_plot+1;
    for i=1:Na;
      neff1(i)=(neffTM-(p(i)*dneff));
      Beff(i)=(2*pi*neff1(i))/lambda;
      Bout=Z*exp(-(ka*zra*x*x)/(2*((f^2)+(zra^2))));
      phi(n,i)=(phis+(BS*(41-(2*i))*warray*x/(2*f))+(Beff(i)*(Lo+((i-1)*dL))));
      phiexp(n,i) = A(i)*Bout*exp(1i*phi(n,i));
    end

    FVABS(n,j)=abs(sum(phiexp(n,:)));
    FVABS2(n,j)=FVABS(n,j)*FVABS(n,j);
    OUTCOUPLE(n,j)=Ey1(n)*FVABS(n,j);
    x=x+extraoutput;
   end
```

```
    x=linspace((do-(wot)),(do+(wot)),count_plot+1);
    yy=trapz(x,OUTCOUPLE(:,j));
    yyy=trapz(x,FVABS2(:,j));
    C(j)=(yy*yy)/(Amp*yyy);
    CC(j)=C(j)*yyy;
    y(j)=10*log10(CC(j)/sum(L));
    lambda=lambda+tunelambda;
    H(j,k)=y(j);
    k
    j
    end

  q=lambdastart:tunelambda:lambdastop;
  plot(q,y);
  hold on;
  do=do+woutput;
end
toc;

                         %%%%%%%%%%%%%% OUTPUT FPR ENDS %%%%%%%%%%

            %%%%%%%%%%%%%%%%%%%%% PROGRAM ENDS %%%%%%%%%%%%%%%%%%%%%%%%%%%%
```

REFERENCES

[1] W. Bogaerts, P. De Heyn, T. Van Vaerenbergh, K. De Vos, S. Kumar Selvaraja, T. Claes, P. Dumon, P. Bienstman, D. Van Thourhout, and R. Baets, "Silicon microring resonators," *Laser & Photonics Reviews*, vol. 6, no. 1, pp. 47–73, 2012.

[2] S. Xiao, M. H. Khan, H. Shen, and M. Qi, "Silicon-on-insulator microring add-drop filters with free spectral ranges over 30 nm," *Journal of Lightwave Technology*, vol. 26, no. 2, pp. 228–236, 2008.

[3] R. Grover, V. Van, T. Ibrahim, P. Absil, L. Calhoun, F. Johnson, J. Hryniewicz, and P. Ho, "Parallel-cascaded semiconductor microring resonators for high-order and wide-FSR filters," *Journal of Lightwave Technology*, vol. 20, no. 5, pp. 900–905, 2002.

[4] M. A. Popovíc, T. Barwicz, M. R. Watts, P. T. Rakich, L. Socci, E. P. Ippen, F. X. Kärtner, and H. I. Smith, "Multistage high-order microring-resonator add-drop filters," *Optics Letters*, vol. 31, no. 17, pp. 2571–2573, 2006.

[5] S. Xiao, M. H. Khan, H. Shen, and M. Qi, "A highly compact third-order silicon microring add-drop filter with a very large free spectral range, a flat passband and a low delay dispersion," *Optics Express*, vol. 15, no. 22, pp. 14 765–14 771, 2007.

[6] J. Niehusmann, A. Vörckel, P. H. Bolivar, T. Wahlbrink, W. Henschel, and H. Kurz, "Ultrahigh-quality-factor silicon-on-insulator microring resonator," *Optics Letters*, vol. 29, no. 24, pp. 2861–2863, 2004.

[7] P. Pan, J. An, L. Wang, Y. Wu, Y. Wang, X. Hu *et al.*, "Design and fabrication of an InP arrayed waveguide grating for monolithic PICs," *Journal of Semiconductors*, vol. 33, no. 7, p. 074010, 2012.

[8] H. M. Kim, D. C. Kim, J. S. Kim, J. H. Kim, K. E. Pyun, S. G. Kang, H. R. Choo, and K.-H. Yoo, "Design and fabrication of an 8-channel InP arrayed waveguide grating demultiplexer module with wide tuning range," *JOURNAL-KOREAN PHYSICAL SOCIETY*, vol. 38, no. 3, pp. 173–176, 2001.

[9] X. Zhang, R. Zhang, D. Lu, B. Wang, and C. Ji, "Design and fabrication of an InP-based arrayed waveguide grating," in *Asia Communications and Photonics Conference*. Optical Society of America, 2013, pp. AF2B–18.

[10] K. Okamoto, K. Takiguchi, and Y. Ohmori, "16-channel optical add/drop multiplexer using silica-based arrayed-waveguide gratings," *Electronics Letters*, vol. 31, no. 9, pp. 723–724, 1995.

[11] H. Nishi, T. Tsuchizawa, T. Watanabe, H. Shinojima, S. Park, R. Kou, K. Yamada, and S.-i. Itabashi, "Monolithic Integration of a Silica-Based Arrayed Waveguide Grating Filter and Silicon Variable Optical Attenuators Based on p–i–n Carrier-Injection Structure," *Applied Physics Express*, vol. 3, no. 10, p. 102203, 2010.

[12] B. Yang, Y. Zhu, Y. Jiao, L. Yang, Z. Sheng, S. He, and D. Daoxin, "Compact arrayed waveguide grating devices based on small SU-8 strip waveguides," *Journal of Lightwave Technology*, vol. 29, no. 13, pp. 2009–2014, 2011.

[13] M. Piels, J. F. Bauters, M. L. Davenport, M. J. Heck, and J. E. Bowers, "Low-Loss Silicon Nitride AWG Demultiplexer Heterogeneously Integrated With Hybrid III–V/Silicon Photodetectors," *Journal of Lightwave Technology*, vol. 32, no. 4, pp. 817–823, 2014.

[14] K. Okamoto, "Athermal silicon photonics array waveguide grating (AWG) employing different core geometries in the array waveguides," Oct. 7 2010, US Patent App. 12/899,715.

[15] X. Fu, L. Jin, Y. Shi, and D. Dai, "Ultra-compact Reflective Si-nanowire Arrayed-waveguide grating (de) multiplexer with Straight Arrayed waveguides and Bragg Reflectors," in *Asia Communications and Photonics Conference*. Optical Society of America, 2013, pp. AF1A–4.

[16] S. Cheung, T. Su, K. Okamoto, and S. Yoo, "Ultra-compact Silicon Photonic 512x512 25-GHz Arrayed Waveguide Grating Router," 2014.

[17] H. Takahashi, K. Oda, and H. Toba, "Impact of crosstalk in an arrayed-waveguide multiplexer on N$\times$ N optical interconnection," *Journal of Lightwave Technology*, vol. 14, no. 6, pp. 1097–1105, 1996.

[18] F. Ohno, K. Sasaki, A. Motegi, and T. Baba, "Reduction in sidelobe level in ultracompact arrayed waveguide grating demultiplexer based on Si wire waveguide," *Japanese Journal of Applied Physics*, vol. 45, no. 8R, p. 6126, 2006.

[19] P. Trinh, S. Yegnanarayanan, F. Coppinger, and B. Jalali, "Silicon-on-insulator (SOI) phased-array wavelength multi/demultiplexer with extremely low-polarization sensitivity," *IEEE Photonics Technology Letters*, vol. 9, no. 7, pp. 940–942, 1997.

[20] D.-J. Kim, J.-M. Lee, J. H. Song, J. Pyo, and G. Kim, "Crosstalk reduction in a shallow-etched silicon nanowire AWG," *IEEE Photonics Technology Letters*, vol. 20, no. 19, pp. 1615–1617, 2008.

[21] A. Prinzen, J. Bolten, M. Waldow, and H. Kurz, "Study on fabrication tolerances of SOI based directional couplers and ring resonators," *Microelectronic Engineering*, vol. 121, pp. 51–54, 2014.

[22] Y. Chu, X. Zheng, H. Zhang, X. Liu, and Y. Guo, "The impact of phase errors on arrayed waveguide gratings," *IEEE Journal of Selected Topics in Quantum Electronics*, vol. 8, no. 6, pp. 1122–1129, 2002.

[23] H. Yamada, K. Okamoto, A. Kaneko, and A. Sugita, "Dispersion resulting from phase and amplitude errors in arrayed-waveguide grating multiplexers–demultiplexers," *Optics Letters*, vol. 25, no. 8, pp. 569–571, 2000.

[24] W.-Y. Chiu, T.-W. Huang, Y.-H. Wu, Y.-J. Chan, C.-H. Hou, H. T. Chien, and C.-C. Chen, “A photonic crystal ring resonator formed by SOI nano-rods,” *Optics Express*, vol. 15, no. 23, pp. 15 500–15 506, 2007.

[25] D.-X. Xu, A. Densmore, P. Waldron, J. Lapointe, E. Post, A. DelÔge, S. Janz, P. Cheben, J. H. Schmid, and B. Lamontagne, “High bandwidth SOI photonic wire ring resonators using MMI couplers,” *Optics Express*, vol. 15, no. 6, pp. 3149–3155, 2007.

[26] X. Wang, W. Shi, H. Yun, S. Grist, N. A. Jaeger, and L. Chrostowski, “Narrow-band waveguide Bragg gratings on SOI wafers with CMOS-compatible fabrication process,” *Optics Express*, vol. 20, no. 14, pp. 15 547–15 558, 2012.

[27] R. Halir, A. Ortega-Moñux, J. G. Wangüemert-Pérez, Í. Molina-Fernández, and P. Cheben, “Fabrication tolerance analysis of bent single-mode rib waveguides on SOI,” *Optical and Quantum Electronics*, vol. 38, no. 9-11, pp. 921–932, 2006.

[28] P. Cheben, J. Schmid, A. DelÔge, A. Densmore, S. Janz, B. Lamontagne, J. Lapointe, E. Post, P. Waldron, and D.-X. Xu, “A high-resolution silicon-on-insulator arrayed waveguide grating microspectrometer with sub-micrometer aperture waveguides,” *Optics Express*, vol. 15, no. 5, pp. 2299–2306, 2007.

[29] B. Gargallo, P. Muñoz, R. Baños, A. L. Giesecke, J. Bolten, T. Wahlbrink, and H. Kleinjans, “Reflective arrayed waveguide gratings based on Sagnac loop reflectors with custom spectral response,” *Optics Express*, vol. 22, no. 12, pp. 14 348–14 362, 2014.

[30] S. Pathak, P. Dumon, D. Van Thourhout, and W. Bogaerts, “Comparison of AWGs and Echelle Gratings for Wavelength Division Multiplexing on Silicon-on-Insulator,” *IEEE Photonics Journal*, vol. 6, no. 5, p. 4900109, 2014.

[31] S. Pathak, D. Van Thourhout, and W. Bogaerts, “Design trade-offs for silicon-on-insulator-based AWGs for (de) multiplexer applications,” *Optics Letters*, vol. 38, no. 16, pp. 2961–2964, 2013.

[32] T. Fukazawa, F. Ohno, and T. Baba, “Very compact arrayed-waveguide-grating demultiplexer using Si photonic wire waveguides,” *Japanese Journal of Applied Physics*, vol. 43, no. 5B, p. L673, 2004.

[33] J. Brouckaert, W. Bogaerts, P. Dumon, D. Van Thourhout, and R. Baets, “Planar concave grating demultiplexer fabricated on a nanophotonic silicon-on-insulator platform,” *Journal of Lightwave Technology*, vol. 25, no. 5, pp. 1269–1275, 2007.

[34] H. Takahashi, S. Suzuki, and I. Nishi, “Wavelength multiplexer based on SiO 2-Ta 2 O 5 arrayed-waveguide grating,” *Journal of Lightwave Technology*, vol. 12, no. 6, pp. 989–995, 1994.

[35] D. C. Kim, H. M. Kim, H. R. Choo, K.-H. Yoo, and T. W. Kim, “Effects of a random variation of the waveguide width on the crosstalk in inp-based arrayed waveguide gratings,” *JOURNAL-KOREAN PHYSICAL SOCIETY*, vol. 38, no. 6, pp. 648–652, 2001.

[36] G. Reed and A. Knights, “Silicon Photonics,” *Wiley publications*, pp. 176–186, 2004.

[37] Cvetojevic, N and Jovanovic, N and Betters, C and Lawrence, J S and Ellis, S C and Robertson, G and Bland-Hawthorn, J, “First starlight spectrum captured using an integrated photonic micro-spectrograph,” *Astronomy and Astrophysics Manuscript*, pp. 1–5, 2012.

[38] D. Feng, N.-N. Feng, C.-C. Kung, H. Liang, W. Qian, J. Fong, B. J. Luff, and M. Asghari, “Compact single-chip VMUX/DEMUX on the silicon-on-insulator platform,” *Optics express*, vol. 19, no. 7, pp. 6125–6130, 2011.

[39] M. R. Pearson, A. Bezinger, A. Delage, J. W. Fraser, S. Janz, P. E. Jessop, and D.-X. Xu, “Arrayed waveguide grating demultiplexers in silicon-on-insulator,” in *Symposium on Integrated Optoelectronics*. International Society for Optics and Photonics, 2000, pp. 11–18.

[40] F. O. Fukazawa, Tatsuhiko and T. Baba, “Very compact arrayed-waveguide-grating demultiplexer using Si photonic wire waveguides,” *Japanese Journal of Applied Physics*, vol. 43, no. 5B, 2004.

[41] D. Dai, S. Liu, S. He, and Q. Zhou, “Optimal design of an MMI coupler for broadening the spectral response of an AWG demultiplexer,” *Journal of Lightwave Technology*, vol. 20, pp. 1957 – 1961, 2002.

[42] S. Selvaraja, W. Bogaerts, D. VanThourhout, and M. Schaekers, “Thermal trimming and tuning of hydrogenated amorphous silicon nanophotonic devices,” *Applied Physics Letters*, vol. 97, pp. 071 120–1 – 071 120–3, 2010.

[43] T. Lipka, M. Kiepsch, H. K. Trieu, and J. MÃijller, “Hydrogenated amorphous silicon photonic device trimming by UV-irradiation,” *Optics Express*, vol. 22, pp. 12 122–12 132, 2014.

[44] “http://optics.synopsys.com/rsoft/rsoft-cad-environment.html.”

[45] S. Chandran and B. K. Das, “Tapering and Size Reduction of Single-Mode Silicon Waveguides by Maskless RIE,” *17th Opto-Electronics and Communications Conference (OECC)*, pp. 655–656, 2012.

[46] G. R. Bhatt, R. Sharma, U. Karthik, and B. K. Das, “Dispersion-free SOI interleaver for DWDM applications,” *Journal of Lightwave Technology*, vol. 30, pp. 140–146, 2012.

[47] S. Harish, D. Venkitesh, and B. K. Das, “Highly efficient DBR in silicon waveguides with eleventh order diffraction,” *SPIE OPTO*, vol. 22, pp. 86 290H–86 290H, 2013.

[48] K. J. Lee and R. Magnusson, “Single-layer resonant high reflector in TE polarization: Theory and experiment,” *Photonics Journal*, vol. 1, pp. 123–129, 2011.

List of publications

1. R. Sidharth and B.K. Das, "Arrayed Waveguide Gratings on 2-μm-SOI for optical interconnects", SPIE Photonics West 2014, Paper No. 8990-12, San Francisco, California, USA, February 2014.

2. R. Sidharth and B.K. Das, "Modeling and Phase Error Analysis of AWG in SOI using Gaussian Beam Approximation", International Conference on Fiber Optics and Photonics, Paper No. T3A.67, IIT Kharagpur, India, December 2014.

3. R. Sidharth and B.K. Das, "Semi - Analytical Model of Arrayed Waveguide Grating in SOI using Gaussian Beam Approximation", Applied Optics 54, pp. 2158-2163, March 2015.